Correspondence to:

K. V. Gamayunov,
kgamayunov@fit.edu

Low Frequency ULF Waves in the Earth's Inner Magnetosphere: Power Spectra During High Speed Streams and Quiet Solar Wind and Seeding of EMIC Waves

Konstantin V. Gamayunov[1] and **Mark J. Engebretson**[2]

[1]Department of Aerospace, Physics and Space Sciences, Florida Institute of Technology, Melbourne, FL, USA, [2]Department of Physics, Augsburg University, Minneapolis, MN, USA

Abstract Here, we extend the scope of the Gamayunov and Engebretson (2021, hereinafter Paper 1), https://doi.org/10.1029/2021JA029247 work by analyzing the low frequency ultra-low-frequency (ULF) wave power spectra in the Earth's inner magnetosphere during high speed stream (HSS) and quiet solar wind (QSW) driving conditions in the upstream solar wind (SW) and comparing our results to the results of Paper 1, where the statistics of ULF wave power spectra during coronal mass ejections (CMEs) are presented. The most important results of our statistical and comparative analyses are as follows. (a) During CMEs, HSSs, and QSW, the magnetic field power spectra of the transverse and compressional fluctuations are well approximated by power laws in the ~mHz–Hz frequency range, where on average the parameters of power law fits during CMEs and HSSs are close, and those during QSW differ considerably from the respective parameters during CMEs and HSSs. (b) The dominance of the average compressional power over the average transverse power for the low frequency ULF waves during the $0 < \text{SYM/H} \lesssim 25$ nT geomagnetic conditions may serve as a proxy of HSSs in the upstream SW, whereas the opposite relation between the average powers is an indication of CMEs. (c) Independently of the SW driving conditions, a turbulent energy cascade from low frequencies in the ULF wave frequency range into the higher frequency range exists in the Earth's inner magnetosphere, supplying the nonthermal electromagnetic seed fluctuations needed for the growth of electromagnetic ion cyclotron waves (~Hz) due to relaxation of unstable distributions of energetic magnetospheric ions.

1. Introduction

Interaction of the upstream solar wind (SW) with Earth's magnetosphere leads to magnetic field fluctuations in a wide ultra-low-frequency (ULF) range from the frequencies of Pc 5 pulsations (2–7 mHz) up to the frequencies of Pc 1 pulsations (0.2–5 Hz). ULF waves in the Pc 4–5 frequency range (2–22 mHz) play an important role in both the energization and loss of radiation belt (RB) relativistic electrons during geomagnetic storms (e.g., Murphy et al., 2018). Compressional Pc 4–5 ULF waves can also affect the growth of electromagnetic ion cyclotron (EMIC) waves, which are generated in the frequency range of Pc 1–2 pulsations (0.1–5 Hz), by modulating the background magnetic field and plasma number density (e.g., Mursula et al., 2001). A nonlinear interaction of transverse ULF waves in the Pc 4–5 frequency range can generate a wave energy cascade from large to small spatial scales, and so this cascade controls the level of nonthermal seed electromagnetic fluctuations in the frequency range of EMIC waves, where EMIC waves can then grow from that nonthermal level if an ion cyclotron instability of the energetic ring current (RC) ion distributions takes place (Gamayunov et al., 2014, 2015). EMIC waves themselves, on the other hand, affect the energetic RC protons (e.g., Gonzalez et al., 1989) and heavy ions (e.g., Thorne & Horne, 1994), thermal electrons (e.g., Cornwall et al., 1971) and ions (e.g., Anderson & Fuselier, 1994), and RB relativistic electrons (e.g., Gamayunov & Khazanov, 2007; Lorentzen et al., 2000; Sandanger et al., 2007), leading to nonadiabatic particle heating and/or pitch-angle scattering in a huge energy range of ~eV-MeV.

The upstream SW conditions are responsible for the physical processes occurring in Earth's magnetosphere, and low frequency ULF waves, in particular, are also driven by conditions in the upstream SW (e.g., Hudson et al., 2004, and references therein). Recognizing this fact and trying to more comprehensively understand and explain observations of the low frequency ULF waves in the Earth's inner magnetosphere, Gamayunov and Engebretson (2021, hereinafter Paper 1) recently suggested to analyze the low frequency ULF waves separately for different SW drivers, and so to systematically study the ULF wave properties as a function of SW drivers.

Paper 1 suggested first to categorize the observed ULF waves according to the upstream SW driving conditions such as coronal mass ejections (CMEs), high speed streams (HSSs), and quiet solar wind (QSW), then analyze the ULF wave properties in each SW driving category, and finally compare wave properties in different categories. Paper 1 was a first attempt to rigorously analyze the power spectra of low frequency ULF waves in the Earth's inner magnetosphere versus different driving conditions in the upstream SW, where the authors applied their approach to the CME driven events. Paper 1 showed that the spectra of both the transverse and compressional ULF waves are well approximated by power laws in a large frequency range of the Pc 1–5 pulsations. This finding is one of the most important ones in Paper 1, because it introduces a new paradigm of a turbulent energy cascade to the physics of Earth's inner magnetosphere. A turbulent energy cascade transfers wave energy from large spatial scales, where most of energy is usually injected to and/or generated in the magnetosphere, to small scales, where the transferred energy is ultimately dissipated by plasma (e.g., Gamayunov et al., 2015, and references therein). In particular, a turbulent energy cascade supplies the nonthermal electromagnetic seed fluctuations into the frequency range of EMIC waves that are needed for EMIC wave growth due to possible instabilities of RC ion distributions. Paper 1 also presented a global view of the low frequency ULF wave power spectra in the inner magnetosphere during CME driving conditions in the upstream SW by providing the most common statistics of ULF wave power. However, despite the fact that the findings of Paper 1 are very important, that paper has a limited scope because only CME driven events were analyzed there. So to fully understand the effects of SW drivers on the ULF wave power spectra, an additional analysis of ULF waves during HSS and QSW conditions is needed along with a subsequent comparison to the results of Paper 1.

The overarching purpose of our study is to extend the scope of Paper 1 by analyzing the low frequency ULF wave power spectra in the Earth's inner magnetosphere during HSS and QSW conditions in the upstream SW and comparing our results to the results of Paper 1 for the CME driven events. Similar to Paper 1, here we also use the database of strongest EMIC wave events observed by the two Van Allen Probes during their first magnetic local time (MLT) revolution (Gamayunov, Elkington, & Engebretson, 2020; Gamayunov, Engebretson, & Elkington, 2020), except the HSS and QSW events are analyzed. This paper is organized similar to Paper 1. In Section 2, we analyze the ULF wave spectra during HSSs by presenting the SYM/H index, Kp index, AE index, MLT, L shell, and magnetic latitude (MLAT) statistics and comparing our results to the respective power spectra during CMEs. In Section 3, we analyze the ULF wave power spectra during QSW conditions and compare them to the results during both CMEs and HSSs. Then, in Section 4, we present the results of our comparative analyses of HSS, CME, and QSW events. Finally, in Section 5, we summarize the major findings of our analyses of the low frequency ULF wave power spectra during CME, HSS, and QSW conditions in the upstream SW.

2. HSS Events: Results and Discussion

2.1. Magnetic Field Data

EMIC waves do not affect the low frequency ULF waves, and so the statistics of low frequency ULF waves cannot depend on whether or not EMIC fluctuations exist in the data analyzed as far as the resulting ULF wave statistics are representative. So for our analysis we use the same data set of the strongest EMIC wave events observed by the two Van Allen Probes during their first MLT revolution from 1 October 2012 through 7 June 2014 (Gamayunov, Elkington, et al., 2020) that was used in Paper 1, except here we analyze the HSS events. This data set was presented and analyzed in the paper by Gamayunov, Engebretson, et al. (2020), where the magnetic field data with the resolution of 64 vectors/s from the Electric and Magnetic Field Instrument Suite and Integrated Science (EMFISIS) observations (Kletzing et al., 2013) were used to produce the data set. Using OMNI data with 5 min time resolution, Gamayunov, Engebretson, et al. (2020) formulated criteria for CME, HSS, and QSW driving conditions in the upstream SW and then categorized EMIC wave events according to the upstream conditions preceding the event. The upstream SW state is identified as HSS if the SW speed V_{sw} grows from the slow SW level ($\lesssim$400 km/s) to the fast SW level ($\sim$500−800 km/s) and peaks of $N_{sw} > 10$ cm^{-3}, $|B| > 10$ nT, and oscillations of B_z with $|B_z| \gtrsim 10$ nT are also observed, and/or V_{sw} has a quasi-plateau at the fast SW level and oscillations in V_{sw} with $\gtrsim$20 km/s peak-to-peak along with oscillations in $|B|$ with $\gtrsim$3 nT peak-to-peak and/or B_z with $\gtrsim$3 nT peak-to-peak are also observed, and/or V_{sw} decreases from the fast to slow SW levels and oscillations in V_{sw} with $\gtrsim$20 km/s peak-to-peak along with oscillations in $|B|$ with $\gtrsim$3 nT peak-to-peak and/or B_z with $\gtrsim$3 nT peak-to-peak are also observed within 18 hr preceding the end of an analyzed EMIC wave event (see Gamayunov, Engebretson, et al., 2020, for more details). The subset of the HSS driven EMIC wave events includes 76 events.
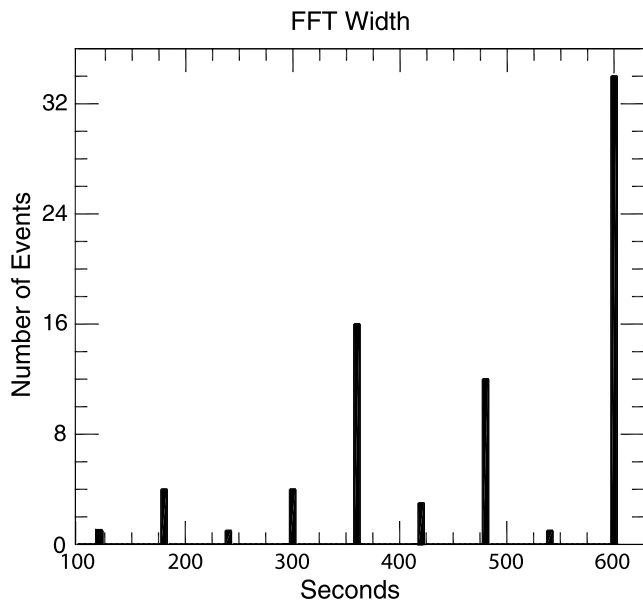
Figure 1. Number of events for each time window used here to calculate the average magnetic field vectors $\langle \mathbf{B_2} \rangle$ and perform FFT analysis for all the 76 HSS events analyzed.

Each of the 76 events is processed according to the methodology described in Paper 1. For convenience, here we briefly outline this methodology as well. First, a 10 min segment of the EMFISIS magnetic field data is taken, where the EMIC wave fluctuations start near the beginning of the segment. The longest wave period that can be identified in each data segment is 10 min, and this corresponds to the lowest ULF wave frequency of 1.67 mHz. Then we calculate the two magnetic field vectors $\langle \mathbf{B_1} \rangle$ and $\langle \mathbf{B_2} \rangle$, where the former vector is obtained by averaging the EMFISIS data over a time window of about 10 EMIC wave periods starting from the beginning of the 10 min segment, and the latter vector is obtained by averaging the EMFISIS data over the entire 10 min segment. If the angle between $\langle \mathbf{B_1} \rangle$ and $\langle \mathbf{B_2} \rangle$ is less than one degree, then vector $\langle \mathbf{B_2} \rangle$ is used to define local field-aligned coordinates (FACs), and the entire 10 min segment is then analyzed. Otherwise, the upper boundary of the 10 min segment is decreased in such a way that a newly defined angle between vector $\langle \mathbf{B_2} \rangle$ recalculated using a decreased segment of data and $\langle \mathbf{B_1} \rangle$ is close to one degree. Then both the recalculated vector $\langle \mathbf{B_2} \rangle$ and decreased segment of EMFISIS data are used for the definition of FACs and the following analysis. Figure 1 shows the histogram of time windows used to calculate the average magnetic field vectors $\langle \mathbf{B_2} \rangle$ for all the 76 HSS events analyzed here. As follows from Figure 1, 34 events (~45%) have the largest time window of 10 min, 12 events (~16%) have the time window of 8 min, 16 events (~21%) have the time window of 6 min, and only one event (~1%) has the smallest time window of 2 min. The numbers of events with other time windows between 2 and 10 min do not exceed 4 events, totaling to ~17%. Second, the segment of the EMFISIS magnetic field data is rotated into the local FACs, where the z-axis is parallel to $\langle \mathbf{B_2} \rangle$, the y-axis is perpendicular to the z-axis in the eastward azimuthal direction, and the x-axis is perpendicular to the z-y plane in the radial direction. Finally, the background magnetic field variation due to spacecraft orbital motion is removed from the 10 min (or less) segment using the least squares fit of a third-order polynomial, and an FFT is separately applied to the detrended B_x, B_y, and B_z time series of data during the entire analyzed segment.

2.2. Power Law Spectra of ULF Waves

Figure 2 shows the magnetic field data in local FACs during the HSS event measured by Van Allen Probe-A during UT = 21:13–21:23 on 14 October 2013. The detrended B_x, B_y, and B_z magnetic field component time series are shown in Figures 2a–2c. Figure 2d shows the power spectrum of fluctuations transverse to the average magnetic field. The dotted lines mark the gyrofrequencies of O^+ and He^+, and the dashed line shows the least squares fit to the power spectrum in the frequency range from 1.67 mHz to 0.25 Hz. The parameters of the power law fit and the Pearson correlation coefficient between power law and observation are given in the insert. Note that the separate power spectra of the B_x and B_y transverse components are also well approximated by power laws, and the power law spectral indices β for the B_x and B_y spectra are close to each other (Gamayunov et al., 2015). For these two reasons and because our study is an initial one, here we only analyze the total power spectra of transverse fluctuations, that is, the sum of the B_x and B_y power spectra. However, more detailed investigations of the ULF wave properties in the future may require a separate analysis of the B_x and B_y power spectra. Figure 2e is the same as Figure 2d, except for the compressional component B_z. The power spikes at frequency ~0.09 Hz and its harmonics are due to the spacecraft spin, and so they are unphysical. Similar to CME events analyzed in Paper 1, the spectra during the HSS event shown in Figure 2 are also approximated well by power laws in the large frequency range from the lowest frequency of the Pc 5 band up to the Pc 1 band frequencies. Note, however, that the spectra in Figures 2d and 2e show the wave energy injection and/or generation not only in the frequency region of EMIC waves ~0.25–0.6 Hz, which is excluded from the power law fits, but also at the Pc 5 frequencies ~2–5 mHz. This means that the low frequency ULF waves in the Pc 5 frequency range are discrete (e.g., Murphy et al., 2018, 2020). This fact is especially well seen in Figures 2a–2c, where the long period ULF oscillations are obvious. The power laws in Figures 2d and 2e are actually observed in the frequency range between the two injection regions, where one is located in the Pc 5 frequency range and another is located at the Pc 1 frequencies.
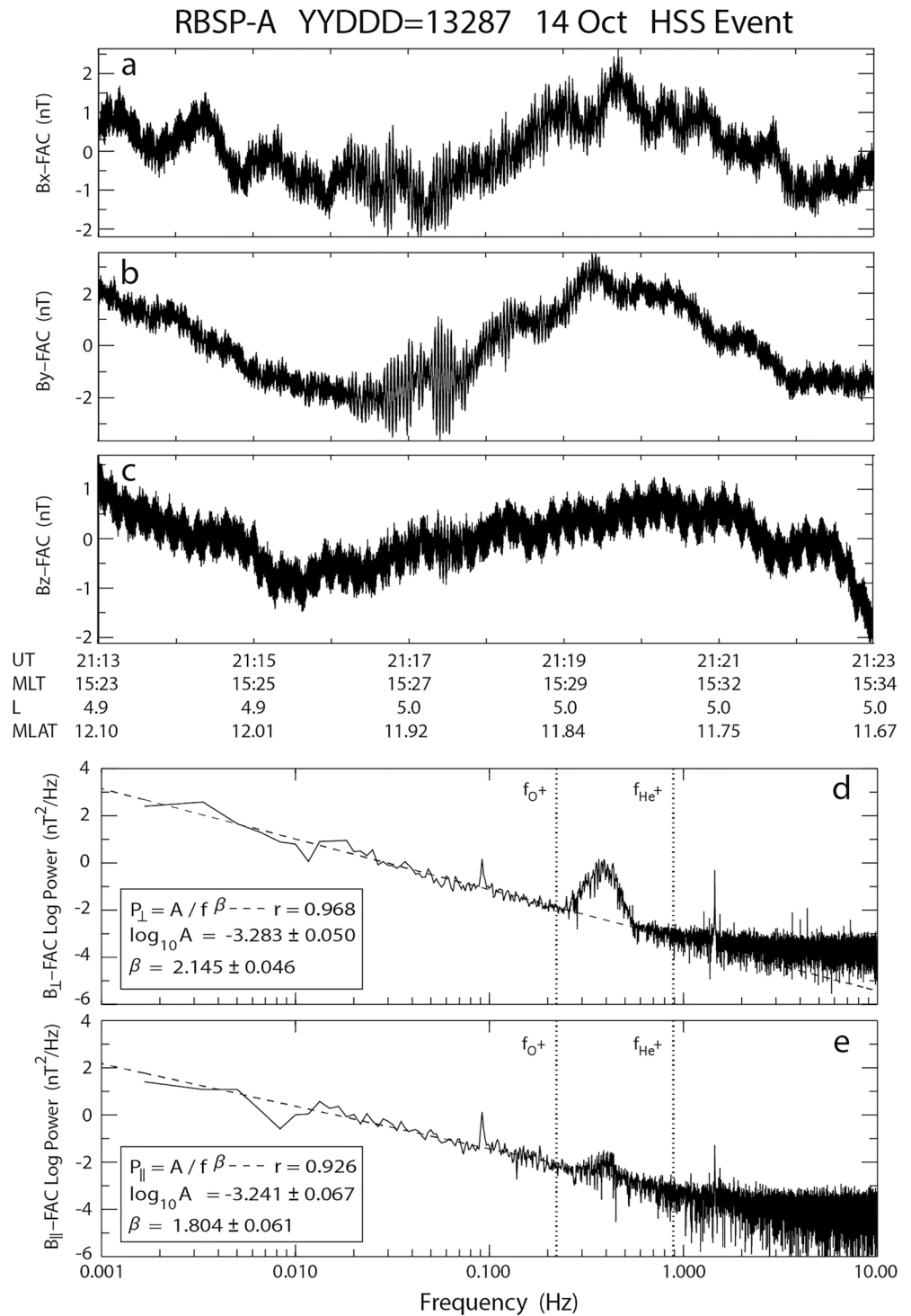
Figure 2. Magnetic field data in local field-aligned coordinates during a HSS event measured by Van Allen Probe-A during UT = 21:13–21:23 on 14 October 2013. (a–c) The detrended B_x, B_y, and B_z magnetic field component time series. (d) The power spectrum of magnetic field fluctuations transverse to the average magnetic field. The vertical dotted lines show the gyrofrequencies of O^+ and He^+ at the time of maximum EMIC wave power. The dashed line shows the least squares fit to the power spectrum in the frequency range from 1.67 mHz to 0.25 Hz. The parameters of the power law fit and the Pearson correlation coefficient r are given in the insert. (e) Same as panel (d), except for B_z.

Following the methodology of Paper 1, however, here we included the low frequency region of the ULF wave energy injection in the calculations of parameters of the power law fits. For both the transverse and compressional spectra the Pearson correlation coefficients are very high, where $r \approx 0.97$ and $r \approx 0.93$ for the transverse and compressional fluctuations, respectively.

Our analysis of all the 76 HSS events confirms that power laws fit well all the observed spectra in the Pc 1–5 frequency range, except one event which we removed from the fits due to a very strong distortion of power spectra by the spin induced signal. Similar to Paper 1, in our analysis here we also did not separate fluctuations on the basis of whether they are discrete or broadband in the low frequency part of the ULF wave spectra. Note, however, that the majority of the events analyzed are discrete in the Pc 4–5 frequency range, and power laws are observed in the frequency range between the two energy injection regions in the Pc 4–5 and EMIC wave frequency ranges, similar to that in Figure 2. So the low frequency ULF wave spectra during HSS events can be approximated by the power law distributions

$$P_{\perp,\parallel}(f) = \frac{A_{\perp,\parallel}}{f^{\beta_{\perp,\parallel}}}, \tag{1}$$

similar to that for CME events analyzed in Paper 1. The notation used in Equation 1 is identical to that in Paper 1. Following the methodology of Paper 1, here we also use Equation 1 to specify the low frequency ULF wave spectra for each event analyzed by the power law spectral density at the frequency $f_{av} = 4.5$ mHz (we actually use $\log_{10} P(f_{av})$) and the respective spectral index β. In other words, a figure similar to Figure 2 is first produced for each event, and then the power law fits are used instead of the FFT spectra to describe the ULF wave spectra for that particular event in the low frequency region where the power law fits are valid. Similar to Paper 1, the highest frequency used in our calculations of the power law parameters is usually taken to be the lowest frequency in the EMIC wave peak in the event analyzed. However, in 19 of the events analyzed (~25% of analyzed events), that frequency is taken slightly below the spacecraft spin frequency of 0.09 Hz to remove the effects of spin signal on the power law parameters. Similar to CME events, observations during HSS conditions show that any of the relationships between the power law spectral indices for the transverse and compressional ULF wave powers can be found, that is, $\beta_\perp \sim \beta_\parallel$, $\beta_\perp \ll \beta_\parallel$, and $\beta_\perp \gg \beta_\parallel$. As was shown in Paper 1, the situation $\beta_\perp \gg \beta_\parallel$ indicates that the Alfvénic fluctuations dominate, whereas the situation $\beta_\perp \ll \beta_\parallel$ is an indication of a dominance of the fast magnetosonic fluctuations, and the situation $\beta_\perp \sim \beta_\parallel$ is observed if there is no clear dominance of any wave mode in the ULF signal.

The observed power law spectra of ULF waves in a large frequency range of the Pc 1–5 pulsations, in combination with the fact that we did not observe shocks and/or discontinuities in the time series of any of the EMFISIS data analyzed, indicates that a turbulent energy cascade in the Earth's inner magnetosphere exists during HSSs, similar to that during CMEs. Despite the well-known fact that the Earth's plasma sheet shows turbulent behavior (e.g., Borovsky et al., 1997; El-Alaoui et al., 2013; Weygand et al., 2005, and references therein), we are not aware of any publications on turbulence in the Earth's inner magnetosphere, except the paper by Gamayunov et al. (2015) and Paper 1, where a new paradigm of a turbulent energy cascade in the Earth's inner magnetosphere was introduced and discussed for the first time.

2.3. Statistics on the SYM/H Index

Following the methodology of Paper 1, we use the 5 min SYM/H index to characterize the intensity of the magnetospheric RC. Figure 3 presents statistics of ULF waves during HSSs on SYM/H. Figures 3a and 3b show $\log_{10} P_\perp(f_{av})$, where $P_\perp$ is in units of nT^2/Hz, and spectral index in the power law spectrum of transverse fluctuations, respectively. Figures 3c and 3d show the same as in Figures 3a and 3b, except for compressional fluctuations. The power law parameters for each event analyzed are shown by the "sample" blue points, the average parameters are shown by the "average" red lines, and the standard deviations are shown by the two "average $\pm$SD" black lines. The -75 nT $\leq$ SYM/H < -50 nT and 25 nT $\leq$ SYM/H < 50 nT bins in Figure 3 include only two events and one event, respectively, and so the statistics in these bins are unreliable. We show these bins only to specify the SYM/H range in our database of HSS events. In this and the following sections, the standard deviation is calculated as the square root of total variance. The total variance, on the other hand, is calculated as a sum of two variances. The first variance is due to errors in the individual power law fits and characterizes the standard deviation of the average, whereas the second variance is due to scattering of sample points with respect
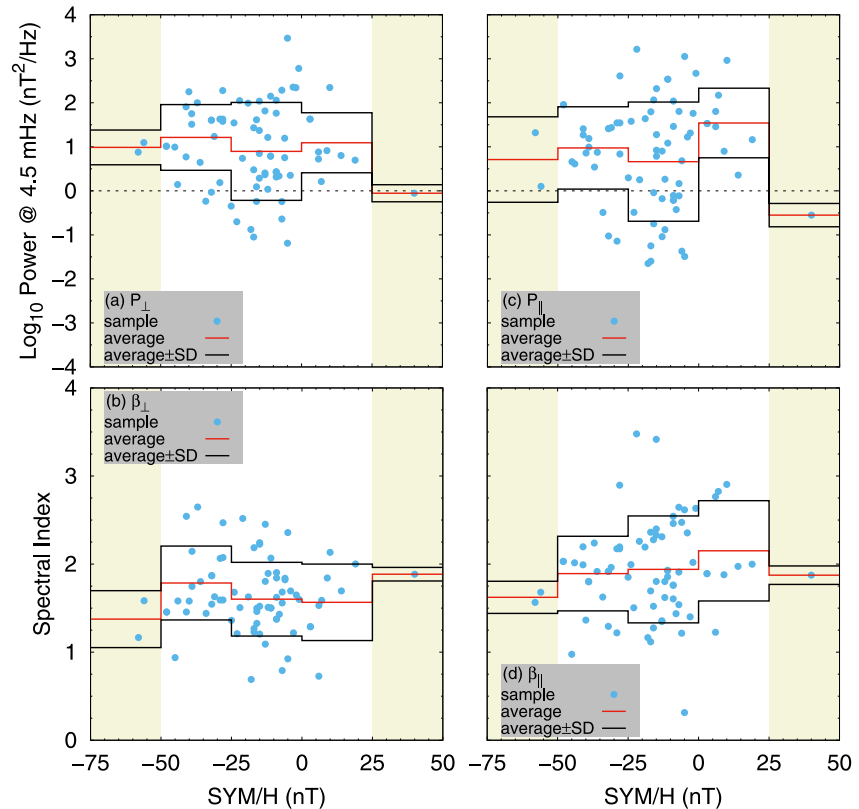
Figure 3. Parameters of the power law fits to the magnetic field spectra of ultra-low-frequency waves during high speed stream (HSS) conditions as a function of SYM/H. (a) Logarithm of the power law spectrum of transverse fluctuations at 4.5 mHz. (b) Spectral index in the power law spectrum of transverse fluctuations. (c and d) Same as panels (a and b), except for compressional fluctuations. The power law parameters for each event analyzed are shown by the "sample" blue points, the average parameters are shown by the "average" red lines, and the standard deviations are shown by the two "average ±SD" black lines. Note that the −75 nT ≤ SYM/H < −50 and 25 nT ≤ SYM/H < 50 nT bins (they are filled with beige) include two events and one event, respectively, and so the statistics in these bins are unreliable. We show these bins only to specify the SYM/H range in our database of HSS events.

to the average. The latter variance strongly dominates the former one in all the reliable bins. Also, here we analyze the SYM/H dependencies using the average parameters, and our analyses in the following sections focus on the average parameters as well.

In both Figures 3a and 3c, the minima of the average ULF wave powers are located in the bin −25 nT ≤ SYM/H < 0, where both powers are close, being $\langle \log_{10} P_{\perp} \rangle = 0.9$ and $\langle \log_{10} P_{\parallel} \rangle = 0.7$. The power maxima in the lowest reliable bin of −50 nT ≤ SYM/H < −25 nT are also close, where $\langle \log_{10} P_{\perp} \rangle = 1.2$ and $\langle \log_{10} P_{\parallel} \rangle = 1$. The average power of the compressional fluctuations in the highest reliable bin of 0 ≤ SYM/H < 25 nT, on the other hand, dominates the average transverse power there, where $\langle \log_{10} P_{\parallel} \rangle = 1.5$ and $\langle \log_{10} P_{\perp} \rangle = 1$. The negative SYM/H indices indicate that an internal magnetospheric source of ULF waves is likely to dominate an external source (see Paper 1 for details). So, as follows from Figures 3a and 3c, an internal source during HSS conditions produces the close powers of the transverse and compressional fluctuations, and those powers increase with the intensity of the RC. A qualitatively similar situation also takes place for an internal source of ULF waves during CME conditions as it follows from Figure 4 in Paper 1 (see the region −50 nT ≤ SYM/H < 0 there). An external source of ULF waves, which dominates during the positive SYM/H indices, operates differently during HSSs and CMEs. During HSS conditions, both the transverse and compressional powers increase in the bin 0 ≤ SYM/H < 25 nT, where the compressional fluctuations are substantially more powerful than the transverse ones. During CME conditions, on the other hand, both the transverse and compressional powers decrease in the bin 0 ≤ SYM/H < 25 nT (see Figure 4 in Paper 1). The observed qualitative difference in the operation of an external source during HSSs and CMEs is mainly due to the fact that the SW speed is always at the fast SW level during HSSs, whereas it is frequently at the slow SW level during CMEs (e.g., Gamayunov, Engebretson, et al., 2020). As a consequence,

the dayside magnetopause compression, which leads to the positive SYM/H indices, is caused by the fast low density SW during HSSs, whereas compression during CMEs is frequently caused by the dense ejecta in the slow SW. So an external source of ULF waves due to the Kelvin-Helmholtz instability along the magnetopause flanks is significantly stronger during HSSs, when the SW is fast, than during CMEs, when the SW is frequently slow (e.g., Murphy et al., 2018; Takahashi et al., 2012). In addition, the contribution from an external source during HSS conditions is dominated by the compressional ULF wave power, in contrast to that during CMEs. A contribution into the inner magnetosphere ULF waves from the external source during CMEs is only seen when a high compression of the dayside magnetopause leading to SYM/H > 25 nT takes place (see Figure 4 in Paper 1). All those "high compression" CME events take place during an interplanetary shock or a combination of shock and ejecta, where the SW speed is below the fast SW level. These upstream SW conditions are very different compared to the upstream conditions during HSSs. This may suggest, in combination with the fact that the average powers of transverse and compressional ULF waves are close during the high compression CME events, that a different mechanism, not related to the Kelvin-Helmholtz instability, is responsible for an external source of ULF waves during CME driving conditions. Thus we conclude that (a) the profiles of average ULF wave powers in the region -50 nT $\leq$ SYM/H < 0 are qualitatively close during HSSs and CMEs, (b) an external source of ULF waves during HSSs is clearly seen in the region $0 \leq$ SYM/H < 25 nT, where the average compressional power dominates the average transverse one, whereas an external source during CMEs is only seen in the region SYM/H > 25 nT, where the average transverse and compressional powers are close, and (c) the dominance of the average compressional power over the average transverse power during the $0 <$ SYM/H $\lesssim 25$ nT conditions may serve as a proxy of HSSs in the upstream SW, whereas the opposite relation between the average powers is an indication of CMEs.

From Figures 3b and 3d, the following three conclusions can be formulated. (a) For both the transverse and compressional fluctuations during HSSs, the average spectral indices change weakly in the reliable region of -50 nT $\leq$ SYM/H < 25 nT, where $\langle \beta_\perp \rangle = 1.6$–$1.8$ and $\langle \beta_\parallel \rangle = 1.9$–$2.2$. So the indices during HSSs are close to the respective indices during CMEs shown in Figure 4 of Paper 1. Also similar to Paper 1, the $\langle \beta_\perp \rangle$ index in Figure 3b slightly decreases with SYM/H. In contrast to CMEs, however, the $\langle \beta_\parallel \rangle$ index in Figure 3d increases with SYM/H. It has been shown in Paper 1 that ULF waves generated by the external source have on average larger spectral indices compared to those generated by the internal source. So an increase of $\langle \beta_\parallel \rangle$ in the $0 \leq$ SYM/H < 25 nT bin of Figure 3d is likely due to the fact that an external source during HSS conditions is strong when SYM/H is positive. The absence of similar behavior in Figure 3b may be attributed to a combination of the following two facts. First, the spectral index decrease or increase is weak in Figures 3b and 3d and second, the external source during HSSs is dominated by the compressional ULF fluctuations. The second and third conclusions here are qualitatively similar to the respective conclusions formulated in Paper 1 for the CME driven events. These conclusions are (b) on average the spectral indices for compressional power are larger than the indices for transverse power, indicating that the fast magnetosonic fluctuations dominate the Alfvénic fluctuations in the observed ULF signals, and (c) during the |SYM/H| $\lesssim 25$ nT geomagnetic conditions, the average spectral index for the transverse ULF wave power is $\langle \beta_\perp \rangle = 1.6$, which is close to the spectral index of 5/3 for the power spectrum of Kolmogorov turbulence.

2.4. Statistics on the *Kp* Index

To analyze statistics of the low frequency ULF wave power spectra on the *Kp* index, we show in Figure 4 the parameters of power law fits to the magnetic field spectra of ULF waves during HSSs as a function of the 3 hr *Kp*. The *Kp* indices are calculated here similar to those in Paper 1. Figures 4a and 4b show the parameters of power law fits for transverse fluctuations, and Figures 4c and 4d show the fit parameters for compressional fluctuations. The highest $5 \leq Kp < 6$ and $6 \leq Kp < 7$ bins are removed from our analysis because the statistics there are unreliable.

The average powers in Figures 4a and 4c monotonically increase with *Kp* across the reliable *Kp* < 5 range. The powers here are close to the respective powers during CMEs shown in Figure 5 of Paper 1, where a detailed discussion of the power *Kp* dependencies is presented. During HSSs, the transverse power dominates the compressional power in the lowest *Kp* < 3 bin, where $\langle \log_{10} P_\perp \rangle = 0.5$ and $\langle \log_{10} P_\parallel \rangle = 0.02$. So similar to CMEs, the average transverse power dominates the average compressional power during geomagnetically quiet periods under HSSs (*Kp* ∼ 3 separates the quiet and disturbed geomagnetic conditions (e.g., Gamayunov, Engebretson,
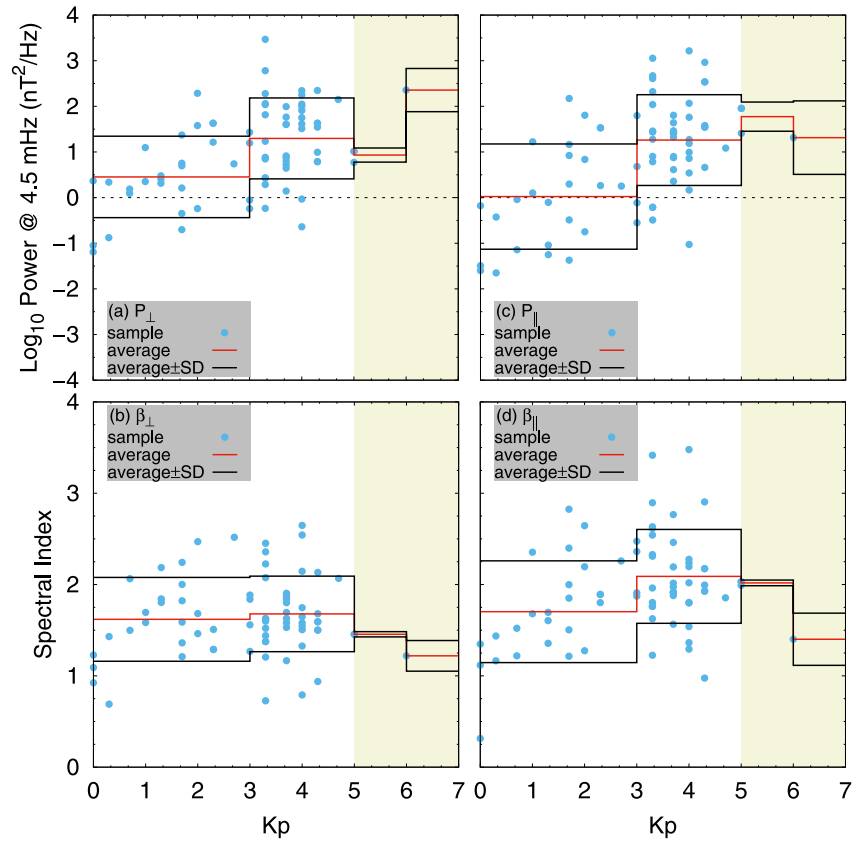
Figure 4. Same as in Figure 3, except as a function of *Kp*. The two highest $5 \leq Kp < 6$ and $6 \leq Kp < 7$ bins (they are filled with beige) have only two events and one event, respectively, and so the statistics in these bins cannot be considered as reliable. We show these bins only to specify the *Kp* index range in our database of HSS events.

et al., 2020)). In the highest reliable $3 \leq Kp < 5$ bin, the average transverse and compressional powers are close, being $\langle \log_{10}P \rangle = 1.3$. Thus we conclude that the average transverse and compressional ULF wave powers during HSSs are close to the respective powers during CMEs in the moderate $Kp < 5$ range shared by the CME and HSS events.

From Figures 4b and 4d the following three conclusions can be drawn. (a) The average spectral indices during HSSs monotonically grow with *Kp* for both the transverse and compressional powers in the reliable *Kp* range. This growth is qualitatively similar to the spectral index growth during CMEs. The average indices here are in the ranges of $\langle \beta_\perp \rangle = 1.6\text{–}1.7$ and $\langle \beta_\parallel \rangle = 1.7\text{–}2.1$. So the average indices during HSSs are close to the respective average indices during CMEs shown in Figure 5 of Paper 1. The second conclusion here is also similar to the respective second conclusion for the CME events in Paper 1, that is, (b) the average indices for compressional power are larger than the average indices for transverse power, indicating the dominance of the fast magnetosonic mode over the Alfvénic mode in the low frequency ULF wave signals during HSSs. The third conclusion for HSSs, however, is qualitatively different compared to that during CMEs. The third conclusion here is (c) the average spectral index for transverse power is $\langle \beta_\perp \rangle = 1.6\text{–}1.7$ in the entire reliable $Kp < 5$ region, and it is close to 5/3 for the spectrum of Kolmogorov turbulence. Moreover, the average spectral index for compressional power is also close to the Kolmogorov spectral index, but only in the $Kp < 3$ bin, where $\langle \beta_\parallel \rangle = 1.7$. In contrast to this last conclusion, the Kolmogorov spectral index during CMEs is only observed for transverse fluctuations and only during quiet geomagnetic conditions when $Kp < 3$. These qualitative differences suggest that Kolmogorov turbulence is more common during HSSs compared to that during CMEs, turbulence is more strongly controlled by the SW driving conditions than geomagnetic conditions, and the dominance of the fast magnetosonic mode over the Alfvénic mode during geomagnetically quiet times is weaker during HSSs compared to that during CMEs.
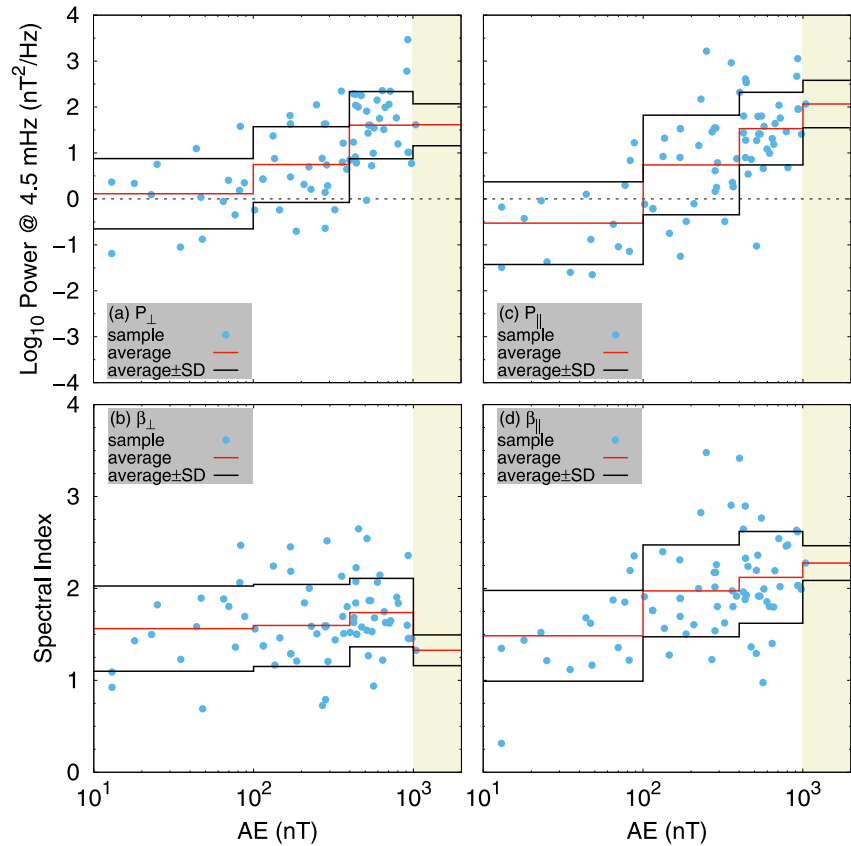
Figure 5. Same as in Figure 3, except as a function of AE. Here the 1,000 nT ≤ AE < 2,000 nT bin (it is filled with beige) has only one event, and so the statistics in this bin cannot be considered as reliable. We show this bin only to specify the AE range in our database of high speed stream events.

2.5. Statistics on the AE Index

Figure 5 shows the parameters of power law fits to the magnetic field spectra of ULF waves during HSSs as a function of the 5 min AE index. The AE indices are calculated here similar to those in Paper 1. Figures 5a and 5b show the parameters of power law fits for transverse fluctuations, and Figures 5c and 5d show the fit parameters for compressional fluctuations. The highest 1,000 nT ≤ AE < 2,000 nT bin has only one event, and this bin is removed from the analysis below because the statistics in this bin are unreliable.

The AE dependencies in Figures 5a and 5c are qualitatively similar to the *Kp* dependencies in Figures 4a and 4c. The average transverse and compressional powers here are close in the 100 nT ≤ AE < 400 nT bin and 400 nT ≤ AE < 1,000 nT bin, where $\langle \log_{10} P \rangle = 0.7$ and $\langle \log_{10} P \rangle = 1.5$–1.6, respectively. These powers are close to the average powers in the respective AE bins during CMEs shown in Figure 6 of Paper 1. A strong power increase in Figures 5a and 5c around AE = 400 nT is similar to that during CMEs. A qualitative difference between the HSS-driven and CME-driven ULF wave powers takes place in the lowest 10 nT ≤ AE < 100 nT bin. Both the average transverse and compressional powers during CMEs weakly depend on AE in the region of AE < 400 nT (see Figure 6 in Paper 1), whereas a strong power increase between the 10 nT ≤ AE < 100 nT bin and 100 nT ≤ AE < 400 nT bin takes place for both the transverse and compressional fluctuations during HSSs. The average powers in the lowest 10 nT ≤ AE < 100 nT bin of Figures 5a and 5c are $\langle \log_{10} P_\perp \rangle = 0.1$ and $\langle \log_{10} P_\parallel \rangle = -0.5$. The observed qualitative difference between the ULF wave power profiles in the region of low substorm activity (AE ≲ 400 nT) during HSSs and CMEs may be caused by the electric field of magnetospheric convection, which is larger during CMEs than during HSSs. A larger magnetospheric convection results in an elevated ion injection, and so RC enhancement, during CME-driven events. This supports the local generation of ULF waves at the low substorm activity level AE ≲ 100 nT during CMEs, in contrast to that during HSSs. The average transverse power dominates the average compressional power in the lowest AE < 100 nT bin during
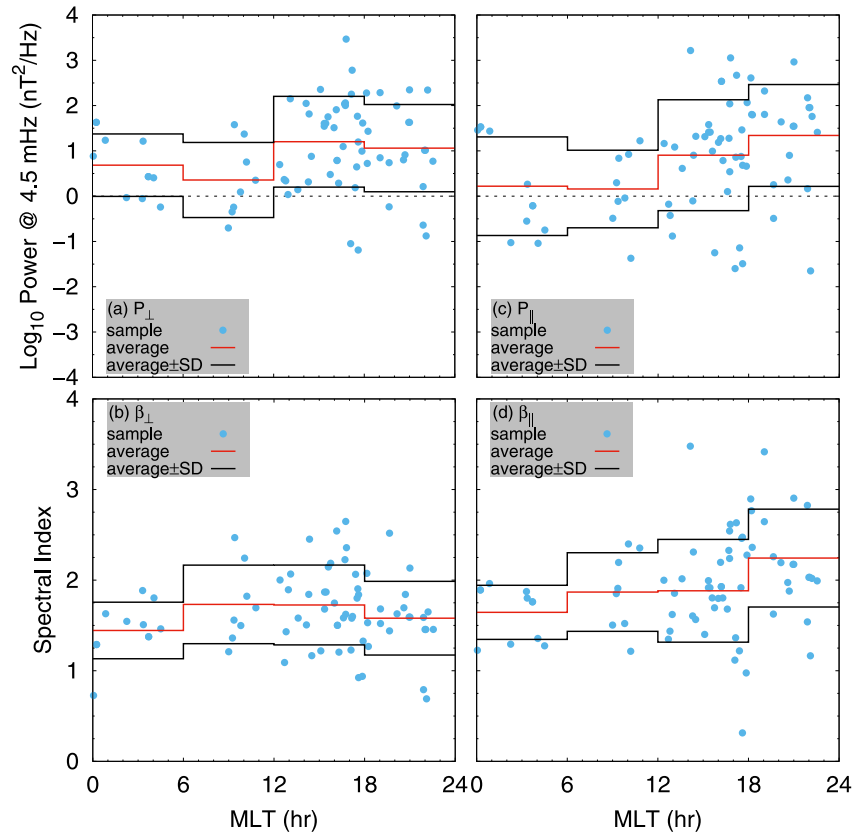
Figure 6. Same as in Figure 3, except as a function of magnetic local time (MLT).

HSSs, similar to that during CMEs. Thus we conclude that the average transverse and compressional ULF wave powers during HSSs are close to the respective powers during CMEs in the 100 nT $\leq$ AE < 1,000 nT range, whereas the average powers in the range of 10 nT $\leq$ AE < 100 nT are about 3–5 times lower during HSSs compared to those during CMEs.

The average AE dependencies in Figures 5b and 5d are also similar to those in Figures 4b and 4d. Here, our three conclusions are formulated as follows. (a) The average spectral indices during HSSs grow with AE in all the reliable AE bins, similar to the spectral index growth during CMEs. The average spectral indices in Figures 5b and 5d are in the ranges of $\langle \beta_\perp \rangle = 1.6$–1.7 and $\langle \beta_\parallel \rangle = 1.5$–2.1, respectively. So the average indices during HSSs are close to the respective indices during CMEs shown in Figure 6 of Paper 1. The second conclusion here is also similar to the second conclusion for CMEs, that is, (b) the average indices for compressional power are larger than the average indices for transverse power except the lowest 10 nT $\leq$ AE < 100 nT bin, where $\langle \beta_\parallel \rangle = 1.5$ is slightly below $\langle \beta_\perp \rangle = 1.6$. The difference, however, is small and only takes place during a low level of substorm activity. So the fast magnetosonic mode usually dominates the Alfvénic mode in the ULF fluctuations during HSSs. The third conclusion for HSSs, however, is qualitatively different compared to that during CMEs. The third conclusion here is (c) the average spectral index for transverse fluctuations is $\langle \beta_\perp \rangle = 1.6$–1.7 in the entire reliable 10 nT $\leq$ AE < 1,000 nT region, and it is close to 5/3 for the spectrum of Kolmogorov turbulence. In contrast to this last conclusion, the Kolmogorov spectral index during CMEs is observed only during quiet geomagnetic conditions when AE $\lesssim$ 400 nT. The last conclusion here is qualitatively similar to the last conclusion regarding spectral indices in Section 2.4.

2.6. Statistics on MLT

Figure 6 shows the parameters of power law fits to the magnetic field spectra of ULF waves during HSSs as a function of MLT, where the entire MLT range presented in our data set of HSS events is the same as in Paper 1.

Figures 6a and 6b show the parameters of power law fits for transverse fluctuations, and Figures 6c and 6d show the fit parameters for compressional fluctuations.

For both the average transverse and compressional powers in Figures 6a and 6c, the MLT profiles are qualitatively similar to each other in the 0–18 hr MLT region. In the highest MLT bin of 18–24 hr, however, the average compressional power increases, whereas the average transverse power decreases. During HSSs, the average logarithms of transverse power are $\langle \log_{10} P_\perp \rangle = 0.7, 0.4, 1.2$, and 1.1 in the 0–6, 6–12, 12–18, and 18–24 hr MLT bins, respectively, and for compressional power the respective averages are $\langle \log_{10} P_\parallel \rangle = 0.2, 0.2, 0.9$, and 1.3. The observed qualitative difference between the MLT profiles for transverse and compressional powers in the 12–24 hr region is likely due to a significant contribution from the external source into the 18–24 hr MLT bin, because the external source of ULF waves is strongly dominated by compressional fluctuations during HSSs (see Figure 3). The MLT profile of compressional power during CMEs is discussed in details in Paper 1. The same physics operates during HSSs, except there is an additional contribution into the 18–24 hr MLT bin from the external source during HSSs. From comparison of the average MLT profile for the compressional ULF wave power during HSSs with the respective profile during CMEs in Figure 7 of Paper 1, we can formulate our first conclusion. (a) The average compressional power during HSSs has a maximum in the 18–24 hr MLT bin, whereas the average compressional power during CMEs has the maximum in the 12–18 hr MLT bin. Qualitatively, to get the average MLT profile for compressional power during HSSs, we have to take the respective average profile during CMEs and then increase the power in the highest 18–24 hr MLT bin by a factor of ~2.5. By comparing the average MLT profile for transverse power during HSSs with the respective profile during CMEs, we can draw our second conclusion. (b) The average transverse power during HSSs has a maximum in the 12–18 hr MLT bin, similar to that during CMEs. However, there is a difference between the MLT locations of the transverse power minima during HSSs and CMEs. Namely, the minimum of transverse power during HSSs is located in the 6–12 hr MLT bin, whereas the power minimum is located in the 0–6 hr MLT bin during CMEs. The average MLT profile of transverse power during CMEs is discussed in Paper 1, and the same physics operates during HSSs as well. To understand the difference in the MLT locations of the transverse power minima during HSSs and CMEs, we have to consider the fact that the magnetosheath ram plasma β_{ram} (the ratio of the ram pressure to the magnetic pressure) is observed below unity, that is, $\beta_{ram} < 1$ about 50–140 times more frequently during CMEs compared to that during HSSs (Borovsky & Denton, 2006). In the case $\beta_{ram} < 1$, the magnetosheath plasma flow has difficulty distorting the magnetic field, which is strong and does not drape around the magnetopause. The strong magnetic field squeezes the magnetosphere, and an asymmetric magnetosheath flow pattern is produced that is very different from the case $\beta_{ram} \gg 1$ (e.g., Borovsky & Denton, 2006). In the case $\beta_{ram} \gg 1$, on the other hand, the magnetosheath flow is little affected by the magnetic field, which is merely convected by the plasma flow. So the magnetosheath flow in the latter case is symmetric with respect to the magnetospheric nose, and a draping of the magnetic field lines over the magnetopause takes place. As a consequence, during CMEs, when the situation $\beta_{ram} < 1$ is more frequent compared to that during HSSs, the transverse ULF wave power downstream of a quasi-parallel bow shock in the prenoon magnetosheath (see Paper 1 for details) is primarily transported along the stiff magnetic field lines because the Alfvén speed there dominates the flow speed. So the downstream transverse power is transmitted into the magnetosphere primarily in the same prenoon MLT sector. During HSSs, on the other hand, the transverse ULF wave power downstream of a quasi-parallel shock is usually convected into the predawn MLT sector by the strong super-Alfvénic magnetosheath flow before ULF waves can reach the magnetopause. So ULF waves are primarily transmitted into the magnetosphere in the predawn MLT sector. This consideration qualitatively explains the difference between the MLT locations of minima for the average transverse powers during HSSs and CMEs.

From Figures 6b and 6d, we draw the following three conclusions. (a) Similar to CMEs, the average spectral index for transverse power during HSSs has a quasi-symmetric MLT-profile with respect to noon, where a maximum of $\langle \beta_\perp \rangle = 1.7$ in the 6–18 hr MLT sector is observed, and the index minima are $\langle \beta_\perp \rangle = 1.4$ and 1.6 in the 0–6 and 18–24 hr MLT bins, respectively. The average transverse indices during HSSs are close to the respective average indices during CMEs shown in Figure 7 of Paper 1. (b) The average spectral index for compressional power during HSSs monotonically grows from $\langle \beta_\parallel \rangle = 1.6$ in the 0–6 hr MLT bin to a quasi-plateau of $\langle \beta_\parallel \rangle = 1.9$ in the 6–18 hr MLT region, and finally to $\langle \beta_\parallel \rangle = 2.2$ in the highest 18–24 hr MLT bin. The major difference between the average indices for compressional powers during HSSs and CMEs is the fact that the index in the 12–18 hr MLT bin is slightly larger during CMEs than that during HSSs. This difference can be understood by considering a combination of the two effects. First, the average spectral indices in the inner magnetosphere are larger
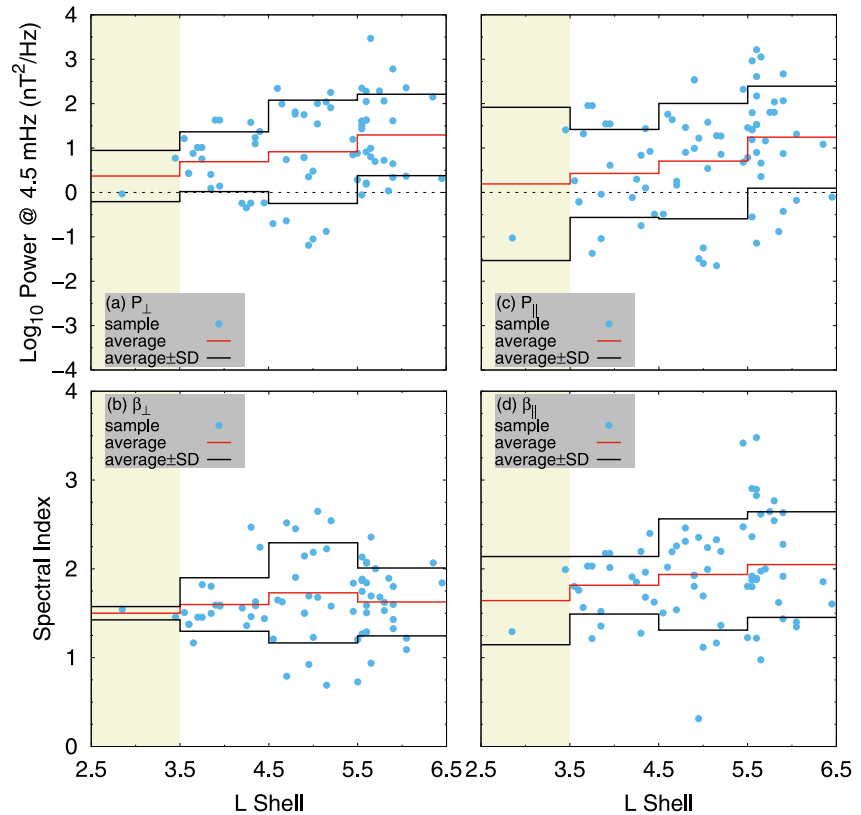
Figure 7. Same as in Figure 3, except as a function of L shell. Here, the $2.5 \leq L < 3.5$ bin (it is filled with beige) has only two events, and so the statistics in this bin cannot be treated as reliable. We show this bin only to specify the L shell range in our database of HSS events.

for the low frequency ULF waves that are supplied by the external sources compared to those for waves that are produced by internal sources (see Paper 1 for more details). Second, the magnetosheath β_{ram} is more frequently observed below unity during CMEs compared to that during HSSs. So during CMEs the compressional ULF wave power downstream of a quasi-perpendicular bow shock in the postnoon magnetosheath (see Paper 1 for details) is more frequently transported perpendicular to the magnetic field, and so reaches the magnetopause in the same postnoon MLT sector. During HSSs, on the other hand, the compressional ULF wave power downstream of a quasi-perpendicular shock is more frequently convected into the postdusk MLT sector by super-Alfvénic magnetosheath flow before ULF waves can reach the magnetopause. So waves during HSSs are usually transmitted into the magnetosphere in the postdusk MLT sector. This consideration qualitatively explains the difference between the average indices for compressional powers in the 12–18 hr MLT bin during HSSs and CMEs. Our third conclusion here is similar to the respective third conclusion for the CME events, that is, (c) during HSSs, the average spectral indices for compressional power are larger than the average spectral indices for transverse power.

2.7. Statistics on L Shell

Figure 7 shows the parameters of power law fits to the magnetic field spectra of ULF waves during HSSs as a function of L shell. In contrast to the CME events analyzed in Paper 1, there are no HSS events in the $2 \leq L < 2.5$ bin in our data set. Figures 7a and 7b show the fit parameters for transverse fluctuations, and Figures 7c and 7d show the same but for compressional fluctuations. The lowest $2.5 \leq L < 3.5$ bin, where only two sample points are observed, is unreliable and removed from our analysis.

The average L shell profiles for the transverse and compressional powers in the reliable $3.5 \leq L < 6.5$ region of Figures 7a and 7c are similar. There are minima in the $3.5 \leq L < 4.5$ bin, where the transverse and compressional powers are $\langle \log_{10} P_\perp \rangle = 0.7$ and $\langle \log_{10} P_\parallel \rangle = 0.4$. Both powers then grow with L shell to $\langle \log_{10} P_\perp \rangle = 0.9$ and $\langle \log_{10} P_\parallel \rangle = 0.7$ in the $4.5 \leq L < 5.5$ bin, and to $\langle \log_{10} P_\perp \rangle = 1.3$ and $\langle \log_{10} P_\parallel \rangle = 1.2$ in the $5.5 \leq L < 6.5$
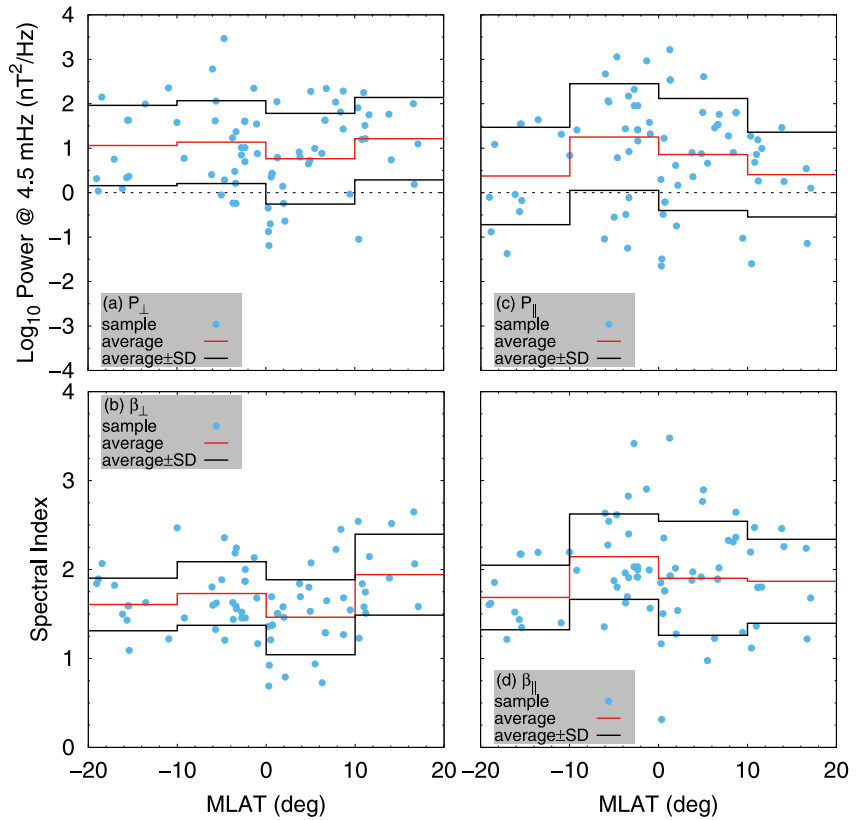
Figure 8. Same as in Figure 3, except as a function of MLAT.

bin. The L shell profiles of average powers during HSSs are close to the respective power profiles during CMEs shown in Figure 8 of Paper 1, except the $5.5 \leq L < 6.5$ bin, where ULF wave powers during HSSs are about 2–2.5 times higher compared to those during CMEs. It is likely that the power minima in Figures 7a and 7c are located just outside the plasmapause (e.g., Takahashi & Anderson, 1992). This, however, cannot be confirmed here because we do not analyze the event locations with respect to the plasmapause. So we only conclude that the average transverse and compressional powers during HSSs are close to the respective powers during CMEs in the $3.5 \leq L < 5.5$ region, whereas the average powers in the $5.5 \leq L < 6.5$ bin are about 2–2.5 times larger during HSSs compared to those during CMEs.

The average L shell profiles in the reliable region of Figures 7b and 7d are similar to the respective spectral index profiles during CMEs shown in Figure 8 of Paper 1. During HSSs, $\langle \beta_\perp \rangle = 1.6$ and $\langle \beta_\parallel \rangle = 1.8$ in the $3.5 \leq L < 4.5$ bin, $\langle \beta_\perp \rangle = 1.7$ and $\langle \beta_\parallel \rangle = 1.9$ in the $4.5 \leq L < 5.5$ bin, and $\langle \beta_\perp \rangle = 1.6$ and $\langle \beta_\parallel \rangle = 2$ in the $5.5 \leq L < 6.5$ bin. The above indices in the $4.5 \leq L < 6.5$ region are slightly below the respective indices during CMEs (see Figure 8 in Paper 1). Similar to CMEs, however, the average spectral indices for compressional power are larger than the indices for transverse power during HSSs as well. So the fast magnetosonic mode also dominates the Alfvénic mode in the low frequency ULF wave signal during HSSs. Thus we conclude that the average spectral indices during HSSs are close to the respective average indices during CMEs in the $3.5 \leq L < 6.5$ range common to both HSS and CME events.

2.8. Statistics on MLAT

Figure 8 shows the parameters of power law fits to the magnetic field spectra of ULF waves during HSSs as a function of MLAT. The MLAT range presented in our data set of HSS events is the same as in Paper 1. Figures 8a and 8b show the fit parameters for transverse fluctuations, and Figures 8c and 8d show the fit parameters for compressional fluctuations.

The compressional power in Figure 8c has a maximum of $\langle \log_{10} P_\parallel \rangle = 1.3$ in the near equatorial bin $-10° \leq \text{MLAT} < 0°$, and the power outside the maximum is in the range of $\langle \log_{10} P_\parallel \rangle = 0.4–0.9$. The transverse power in Figure 8a, on the other hand, has a minimum of $\langle \log_{10} P_\perp \rangle = 0.8$ in the near equatorial bin $0° \leq \text{MLAT} < 10°$, and the power outside this minimum is in the range of $\langle \log_{10} P_\perp \rangle = 1.1–1.2$. These features in the MLAT power profiles during HSSs are qualitatively similar to those during CMEs shown in Figure 9 of Paper 1. However, a qualitative difference between the MLAT power profiles during HSSs and CMEs is also observed. Namely, the north-south asymmetry in the near equatorial region during HSSs is opposite to that during CMEs. The asymmetry during HSSs is mainly due to the probes' orbits, because the magnetosheath flow pressure during HSSs usually dominates the magnetic field pressure there, and so the flow is symmetric with respect to the magnetospheric nose. As a consequence, the near equatorial north-south asymmetry during HSSs reflects a north-south asymmetry due to the Van Allen Probes' orbits, and so that asymmetry is unphysical. During CMEs, on the other hand, the magnetosheath magnetic field pressure frequently dominates the plasma flow pressure, making it difficult for flow to distort magnetic field. The strong magnetic field squeezes the magnetosphere, and an asymmetric magnetosheath flow pattern is produced that is very different from the case of HSSs (Borovsky & Denton, 2006). So the probes' orbital effect may be overshot by the effect of squeezing of the magnetosphere during CMEs, leading to an opposite near equatorial asymmetry in the MLAT power profiles during CMEs compared to that during HSSs. If this is the case, then the asymmetry observed during CMEs is physical at least partly, in contrast to the asymmetry during HSSs. The physics behind a maximum of compressional power in the near equatorial region and a minimum of transverse power there during HSSs is similar to that during CMEs (see Paper 1 for details). The near equatorial minima of the average transverse powers during HSSs and CMEs are close, whereas the maximum of the average compressional power during HSSs is about two times higher compared to that during CMEs. So we conclude that the average MLAT power profiles during HSSs and CMEs are qualitatively similar.

In Figures 8b and 8d, the average spectral indices depend more strongly on MLAT compared to the respective dependencies during CMEs shown in Figure 9 of Paper 1. During HSSs, the average indices for the transverse and compressional powers are in the ranges of $\langle \beta_\perp \rangle = 1.5–1.9$ and $\langle \beta_\parallel \rangle = 1.7–2.1$, respectively. Despite the fact that these index ranges are about 2–4 times wider compared to those during CMEs, the spectral indices averaged over the entire MLAT range are close during both HSSs and CMEs. Also similar to CMEs, the average indices for compressional power dominate the average indices for transverse power during HSSs. Thus we conclude that the average spectral indices during HSSs are qualitatively similar to the respective average indices during CMEs.

2.9. Nonthermal Seed Fluctuations for EMIC Waves

For all the 75 HSS driven events analyzed, the ULF wave spectra are well approximated by power laws in the Pc 1–5 frequency range. Because there are no shocks and/or discontinuities in the time series of all the EMFISIS data analyzed, this indicates that a turbulent energy cascade exists during HSSs, similar to that during CMEs. This cascade supplies the nonthermal electromagnetic seed fluctuations needed for EMIC wave growth due to instabilities of the energetic RC ion distributions. To estimate the transverse seed power in the Pc 1–2 frequency range during HSSs, we use all the 75 events. The estimated seed power is in the range of $P_{\perp,seed,HSS} \sim 10^{-5}–10^{0}$ nT^2/Hz. The range of the EMIC wave seed power during CMEs, on the other hand, is $P_{\perp,seed,CME} \sim 10^{-4}–10^{-1}$ nT^2/Hz (see Paper 1). So we conclude that (a) a turbulent energy cascade exists in the Earth's inner magnetosphere at least in the Pc 1–5 frequency range during both HSSs and CMEs, supplying the nonthermal electromagnetic seed fluctuations needed for EMIC wave growth due to instabilities, and (b) the range of the EMIC wave seed power during CMEs is substantially narrower compared to that during HSSs.

3. QSW Events: Results and Discussion

3.1. Magnetic Field Data

Here, we use the same data set we used in Paper 1 and Section 2, except now we analyze the QSW events. The upstream SW state is identified as QSW if the SW speed $V_{sw} \lesssim 400$ km/s, and there are no interplanetary shocks, and/or ejecta, and/or magnetic clouds during the 18 hr interval before the end of an EMIC wave event analyzed (see Gamayunov, Engebretson, et al., 2020, for more details). Categorization of events using the above criteria results in the 21 QSW events in our data set. Each of those events is processed according to the methodology
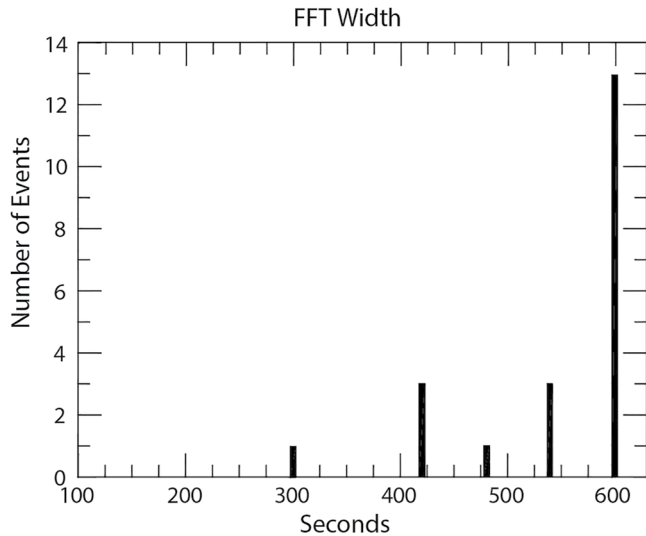
Figure 9. Same as in Figure 1, except for the 21 quiet solar wind events analyzed here.

described in Section 2 and/or Paper 1. Figure 9 shows the time windows used to calculate the vectors of the average magnetic field for all the 21 QSW events analyzed. This figure is similar to Figure 1, except the events during QSW are shown here. As follows from Figure 9, there are 13 events (∼62%) with a 10 min time window, three events (∼14%) with a 9 min time window, one event (∼5%) with an 8 min time window, three events with a 7 min time window, and one event with a 5 min time window.

3.2. Power Law Spectra of ULF Waves

Figure 10 shows the same as in Figure 2, except during the QSW event from 08:42 to 08:52 UT on 9 July 2013. The least squares fits to the power spectra in Figure 10 are performed in the frequency range of 1.67 mHz–0.5 Hz. Similar to the CME events analyzed in Paper 1 and HSS events analyzed in Section 2, the power spectra during QSW event in Figure 10 are also well approximated by power laws in the Pc 1–5 frequency range. Similar to Figure 2, the spectra in Figure 10 have the wave energy injection not only in the frequency range of EMIC waves ∼ 0.5–2 Hz, but also at the Pc 5 frequencies ∼ 2–5 mHz and the Pc 4 frequencies ∼10 mHz. This indicates that the low frequency ULF waves in the Pc 4–5 frequency range are discrete. As before, power laws are observed in the frequency range between the low and high frequency injection regions. For both the transverse and compressional spectra in Figure 10 the Pearson correlation coefficients are very high, where $r \approx 0.84$ and $r \approx 0.94$ for the transverse and compressional fluctuations, respectively.

Analysis of all the 21 QSW events confirms that power laws fit all the power spectra in the Pc 1–5 frequency range, except the two events that we removed from the power law fits because of a very strong distortion of spectra by the spin induced signal. As before, here we also did not separate fluctuations on the basis whether they are discrete or broadband in the low frequency part of the ULF wave spectra. Note, however, that the majority of the events analyzed are discrete in the Pc 4–5 frequency range, and power laws are observed in the frequency range between the low and high frequency injection regions in the Pc 4–5 and EMIC wave frequency ranges. Similar to the CME and HSS events, the ULF wave spectra during QSW can be also approximated by power laws in Equation 1. The highest frequency used in our calculations of the power law parameters is usually taken to be the lowest frequency in the EMIC wave peak in the event analyzed. However, in two events (∼11% of the 19 QSW events analyzed), that frequency is taken slightly below the spacecraft spin frequency of 0.09 Hz to remove the effects of spin signal on the power law parameters. Similar to the CME and HSS events, the relationships $\beta_\perp \sim \beta_\parallel$, $\beta_\perp \ll \beta_\parallel$, and $\beta_\perp \gg \beta_\parallel$ are also represented in the low frequency ULF wave observations during QSW.

We did not observe shocks and/or discontinuities in the time series of any of the EMFISIS data analyzed during the QSW events. So the observed power law spectra of ULF waves in a large frequency range of the Pc 1–5 pulsations indicates that a turbulent energy cascade in the Earth's inner magnetosphere exists during QSW conditions as well, similar to that during both CMEs and HSSs.

3.3. Statistics on the SYM/H Index

Figure 11 shows statistics of ULF waves during QSW on SYM/H. This figure is similar to Figure 3, except the events during QSW are shown. The highest $0 \leq \text{SYM/H} < 25$ nT bin in Figure 11 has only three events, and so the statistics in this bin cannot be considered as reliable. We show this bin only to specify the SYM/H index range in our database of QSW events. Therefore, only one reliable SYM/H index bin is presented in Figure 11, and so the SYM/H index dependencies cannot be analyzed here.

The average transverse and compressional powers in the reliable bin of Figures 11a and 11c are $\langle \log_{10} P_\perp \rangle = -0.2$ and $\langle \log_{10} P_\parallel \rangle = -0.6$, respectively. Similar to the average ULF wave powers in the -25 nT $\leq \text{SYM/H} < 0$ bin during CMEs and HSSs, the transverse power dominates the compressional power during QSW as well. The powers during QSW, however, are significantly lower compared to the respective powers during CMEs and HSSs. Thus we conclude that in the -25 nT $\leq \text{SYM/H} < 0$ region shared by the CME, HSS, and QSW events the average transverse power dominates the average compressional one independently of the SW driving conditions, but the
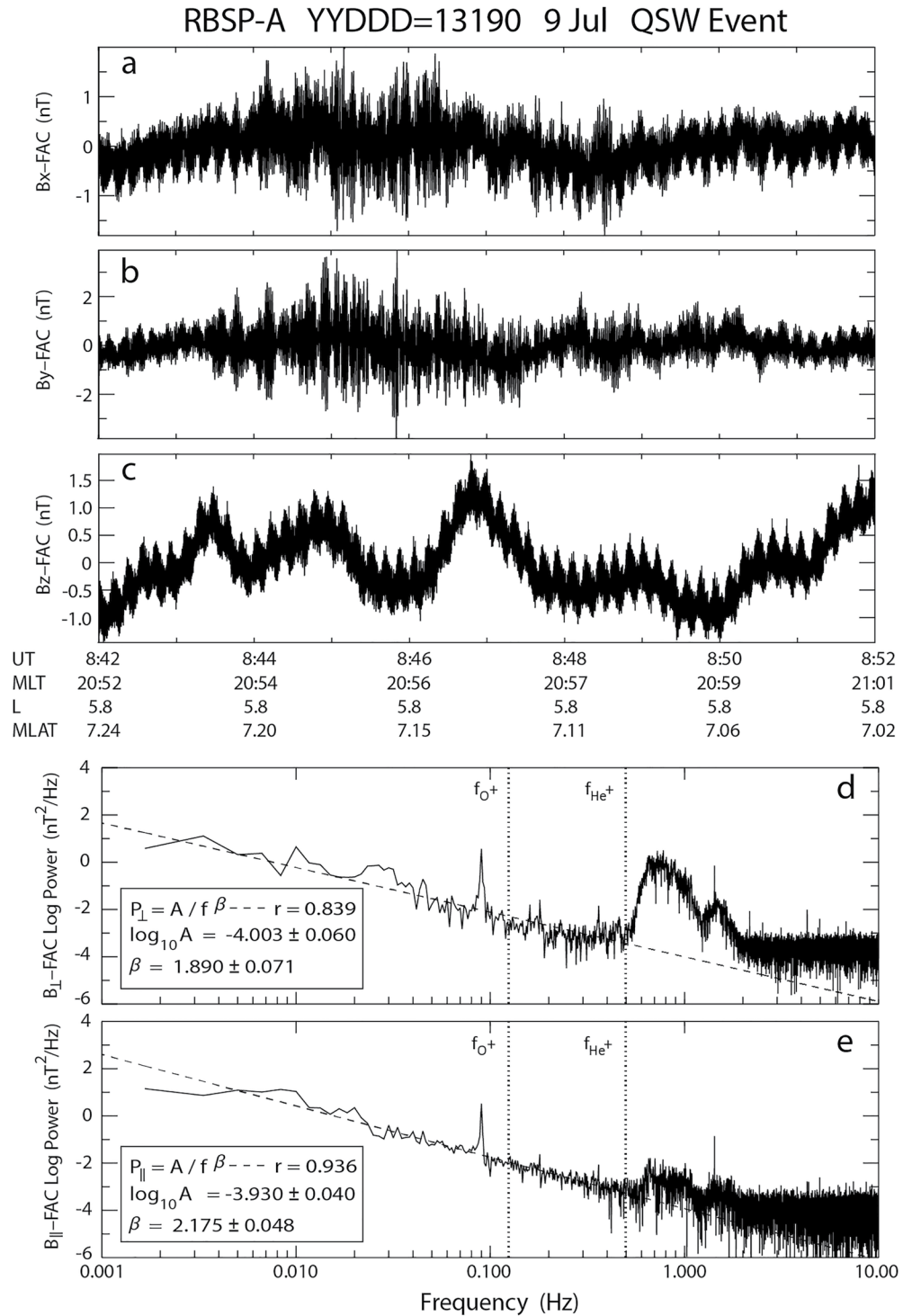
Figure 10. Same as in Figure 2, except during a quiet solar wind (QSW) event from 08:42 to 08:52 UT on 9 July 2013. Note that the least squares fits to the power spectra are performed here in the frequency range of 1.67 mHz–0.5 Hz.

average powers during QSW are about an order of magnitude lower compared to the respective powers during both CMEs and HSSs.

The average spectral indices for the transverse and compressional powers in the -25 nT $\leq$ SYM/H < 0 bin of Figures 11b and 11d are $\langle \beta_\perp \rangle = 1.3$ and $\langle \beta_\parallel \rangle = 1.5$, respectively, and the following two conclusions can be
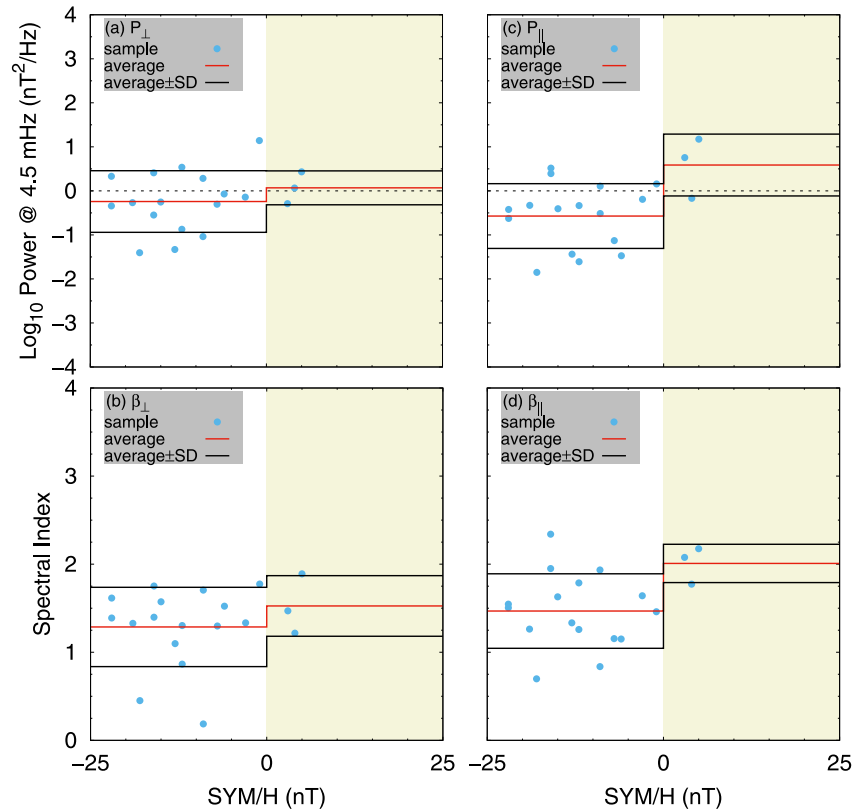
Figure 11. Same as in Figure 3, except during quiet solar wind (QSW). Note that the highest $0 \leq$ SYM/H < 25 nT bin (it is filled with beige) includes only three events, and so the statistics in this bin are unreliable. This bin is shown here only to indicate the entire SYM/H index range presented in our database of QSW events.

formulated. (a) The average spectral indices for the transverse and compressional ULF wave powers during QSW are considerably lower compared to the respective indices during CMEs and HSSs. This is the major difference between the average spectral indices during QSW conditions on the one hand and CME and HSS conditions on the other hand. (b) The average spectral indices for compressional power are larger than the average indices for transverse power during QSW. This conclusion is similar to the respective conclusions during both CMEs and HSSs.

3.4. Statistics on the *Kp* Index

Figure 12 is the same as Figure 4, except the events during QSW are shown. Similar to Section 3.3, the *Kp* index dependencies cannot be analyzed here because only one *Kp* bin is presented. The average ULF wave powers in Figures 12a and 12c are $\langle \log_{10}P_{\perp} \rangle = -0.2$ and $\langle \log_{10}P_{\parallel} \rangle = -0.4$, respectively. Similar to the average powers in the $0 \leq Kp < 3$ bin during CMEs and HSSs, the average transverse power during QSW dominates the compressional one. The powers during QSW, however, are lower compared to the respective powers during CMEs and HSSs. So here we conclude that in the $0 \leq Kp < 3$ bin shared by the CME, HSS, and QSW events the average transverse power dominates the average compressional one independently of the SW driving conditions, but the average powers during QSW are about 3–5 times lower compared to the respective powers during CMEs and HSSs. The average spectral indices in Figures 12b and 12d are $\langle \beta_{\perp} \rangle = 1.3$ and $\langle \beta_{\parallel} \rangle = 1.6$, and our two conclusions here are identical to the respective conclusions in Section 3.3.

3.5. Statistics on the AE Index

Figure 13 is the same as Figure 5, except the events during QSW are shown here. The AE dependencies of the average power profiles in Figures 13a and 13c are qualitatively similar to the AE dependencies during HSSs in
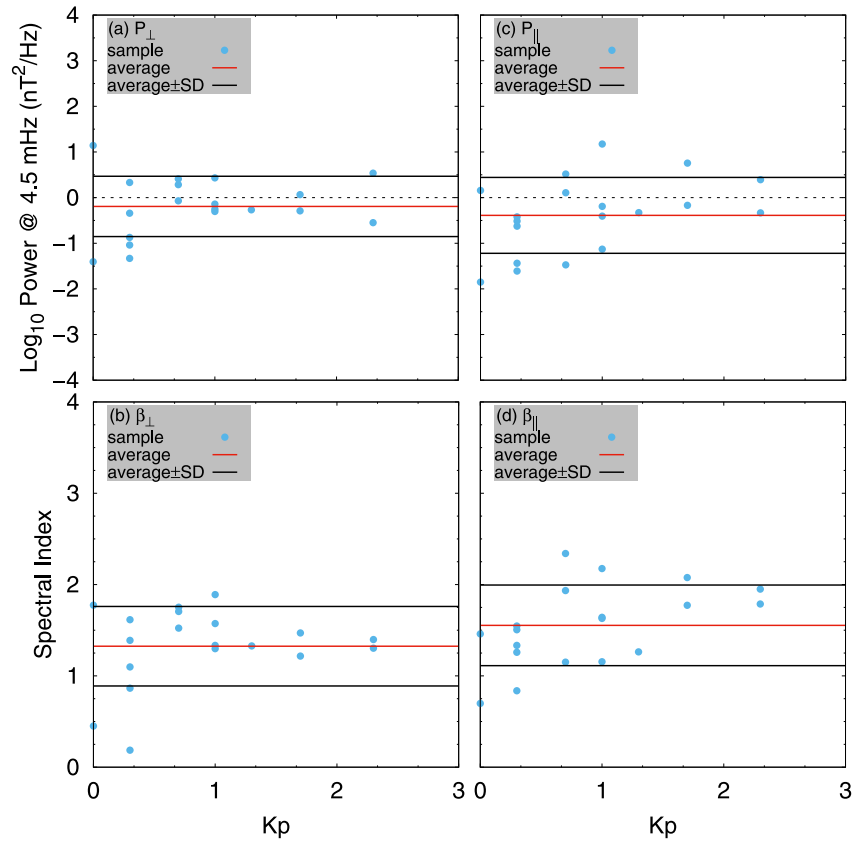
Figure 12. Same as in Figure 4, except during quiet solar wind.

the region 10 nT ≤ AE < 400 nT shown in Figures 5a and 5c. As we discussed in Section 2.5, there is a qualitative difference between the average ULF wave power profiles during HSSs and CMEs in the region of low substorm activity (AE ≲ 400 nT). A similar qualitative difference is also observed between the average AE profiles during QSW and CMEs. The physics that was discussed in Section 2.5 can be also applied here to explain the qualitative difference between the average AE profiles during QSW and CMEs. The average powers in Figures 13a and 13c are $\langle \log_{10}P_\perp \rangle = -0.2$ and $\langle \log_{10}P_\| \rangle = -0.7$ in the lowest 10 nT ≤ AE < 100 nT bin, and $\langle \log_{10}P_\perp \rangle = -0.1$ and $\langle \log_{10}P_\| \rangle = 0$ in the 100 nT ≤ AE < 400 nT bin. Now we can formulate the following two conclusions. (a) In the 10 nT ≤ AE < 400 nT region shared by the CME, HSS, and QSW events, the AE average power profiles during QSW are qualitatively similar to those during HSSs, but not to the profiles during CMEs. (b) The average powers in the lowest 10 nT ≤ AE < 100 nT bin are smaller during QSW compared to the respective powers during HSSs by less than a factor of two. So the average powers during HSSs and QSW are close in the 10 nT ≤ AE < 100 nT bin, whereas the QSW average powers in the 100 nT ≤ AE < 400 nT bin are about 5–6 times lower compared to the HSS average powers there.

The average spectral indices in Figures 13b and 13d depend weakly on the AE index, and they are in the ranges of $\langle \beta_\perp \rangle = 1.3$–1.4 and $\langle \beta_\| \rangle = 1.5$–1.6, respectively. Our two conclusions here are again identical to the respective conclusions in Section 3.3.

3.6. Statistics on MLT

Figure 14 is the same as Figure 6, except the events during QSW are shown. The statistics in Figure 14 are reliable only in the 6–12 hr MLT bin, and the other bins are shown only to specify the MLT range in our database of QSW events. So the MLT dependencies cannot be analyzed here because only one reliable bin is presented.

The average ULF wave powers in the reliable bin of Figures 14a and 14c are $\langle \log_{10}P_\perp \rangle = -0.2$ and $\langle \log_{10}P_\| \rangle = -0.6$, respectively. Similar to the average powers in the MLT = 6–12 hr bin during CMEs and HSSs, the average
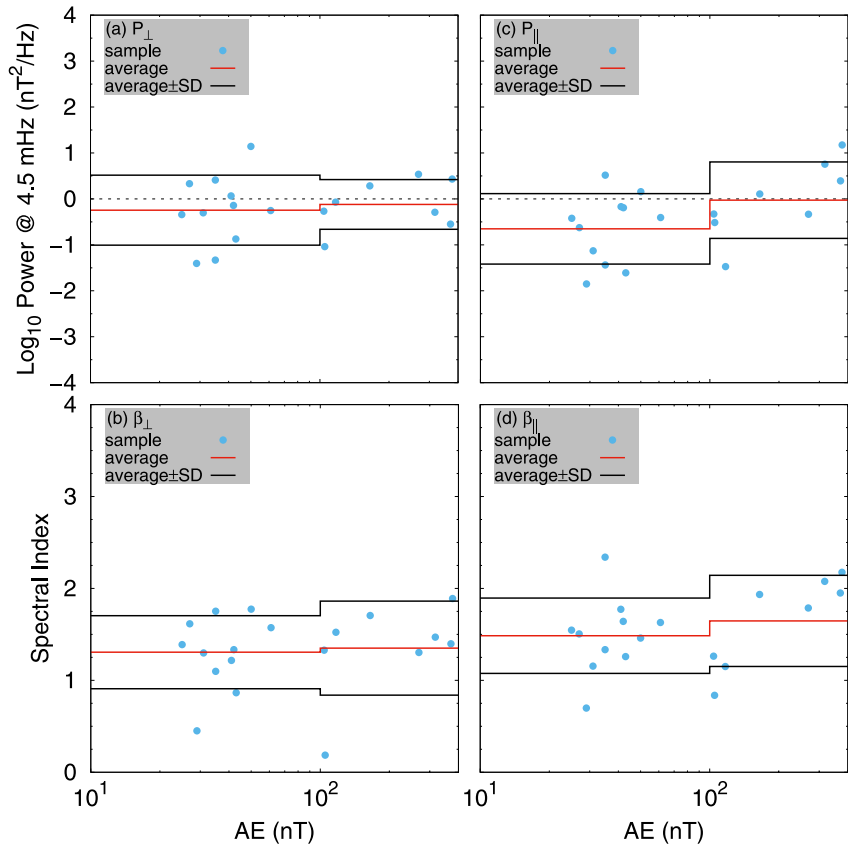
Figure 13. Same as in Figure 5, except during quiet solar wind.

transverse power during QSW dominates the average compressional power. The powers during QSW, however, are substantially lower compared to the respective powers during both CMEs and HSSs. So we conclude that in the MLT = 6–12 hr region shared by the CME, HSS, and QSW events the average transverse power dominates the average compressional power independently of the SW driving conditions, but the average transverse and compressional powers during QSW are about 4–13 times and 6–10 times lower, respectively, compared to the transverse and compressional powers during CMEs and HSSs.

The average spectral indices in the reliable 6–12 hr MLT bin of Figures 14b and 14d are $\langle \beta_\perp \rangle = 1.3$ and $\langle \beta_\parallel \rangle = 1.5$, respectively, and our two conclusions here are identical to the respective conclusions in Section 3.3.

3.7. Statistics on L Shell

Figure 15 is the same as Figure 7, except the events during QSW are shown. The lowest $2.5 \leq L < 3.5$ bin has only one event, and so the statistics in this bin are unreliable. We show this bin only to specify the L shell range in our database of QSW events.

The L shell profile of the average compressional power in the $3.5 \leq L < 6.5$ region of Figure 15c is qualitatively similar to the respective profiles during both CMEs (see Figure 8 in Paper 1) and HSSs (see Figure 7). There is a deep minimum of compressional power in the $3.5 \leq L < 4.5$ bin, where $\langle \log_{10} P_\parallel \rangle = -0.8$ during QSW. From this minimum the QSW compressional power gradually increases with L shell, reaching $\langle \log_{10} P_\parallel \rangle = -0.6$ in the $4.5 \leq L < 5.5$ bin, and $\langle \log_{10} P_\parallel \rangle = -0.1$ in the $5.5 \leq L < 6.5$ bin. The L shell profile of the average transverse power in Figure 15a, on the other hand, is qualitatively dissimilar to the respective power profiles during both CMEs and HSSs. Despite the fact that the average L shell power profiles of the compressional and transverse ULF waves are qualitatively similar during both CMEs and HSSs, the average transverse power during QSW first decreases from $\langle \log_{10} P_\perp \rangle = 0.1$ in the $3.5 \leq L < 4.5$ bin to $\langle \log_{10} P_\perp \rangle = -0.4$ in the $4.5 \leq L < 5.5$ bin, but does not increase as in the case of compressional power, and then almost does not depend on L shell. A qualitative disagreement
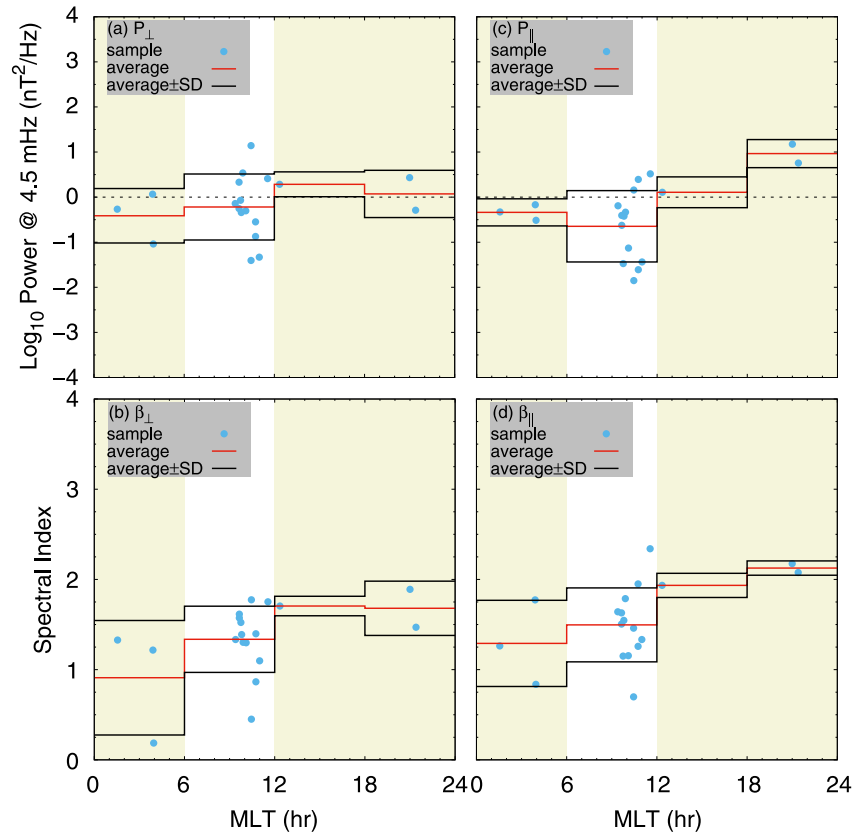
Figure 14. Same as in Figure 6, except during quiet solar wind (QSW). Note that statistics are reliable only in the 6–12 hr MLT bin. The unreliable bins are filled with beige and shown only to specify the MLT range in our database of QSW events.

between the L shell profiles of the average compressional and transverse ULF wave powers during QSW is difficult to explain. Thus we can only formulate the following two conclusions for the region of $3.5 \leq L < 6.5$ shared by the CME, HSS, and QSW events. (a) The L shell profile of the average compressional power during QSW is qualitatively similar to the average compressional power profiles during both CMEs and HSSs. The average powers themselves, however, are about 10–20 times lower during QSW compared to the respective powers during CMEs and HSSs. (b) The L shell profile of the average transverse power during QSW is qualitatively dissimilar to the average transverse power profiles during both CMEs and HSSs, where the CME and HSS profiles grow with L shell, whereas the QSW profile first decreases and then almost does not depend on L shell. Quantitatively, the average transverse powers during QSW are about 2.5–4 times and 25–50 times lower compared to the average transverse powers during CMEs and HSSs in the $3.5 \leq L < 4.5$ and $5.5 \leq L < 6.5$ bins, respectively.

The average spectral indices in the $3.5 \leq L < 6.5$ region of Figures 15b and 15d depend weakly on L shell, being in the ranges of $\langle \beta_\perp \rangle = 1.2$–$1.3$ and $\langle \beta_\parallel \rangle = 1.5$–$1.6$, and our two conclusions here are identical to the respective conclusions in Section 3.3.

3.8. Statistics on MLAT

Figure 16 is the same as Figure 8, except the events during QSW are shown. Here, the $-10° \leq \text{MLAT} < 0°$ bin has only three events, and so the statistics in this bin cannot be considered as reliable. We show this bin only to specify the entire MLAT range in our database of QSW events.

In the reliable bins of Figure 16c, the MLAT profile of the average compressional power is qualitatively similar to the respective compressional power profiles during CMEs (see Figure 9 in Paper 1) and HSSs (see Figure 8). For QSW, the average compressional power has a maximum of $\langle \log_{10} P_\parallel \rangle = 0.3$ in the near equatorial bin of $0° \leq \text{MLAT} < 10°$, and the average power minima are $\langle \log_{10} P_\parallel \rangle = -0.5$ and $\langle \log_{10} P_\parallel \rangle = -0.7$ in the
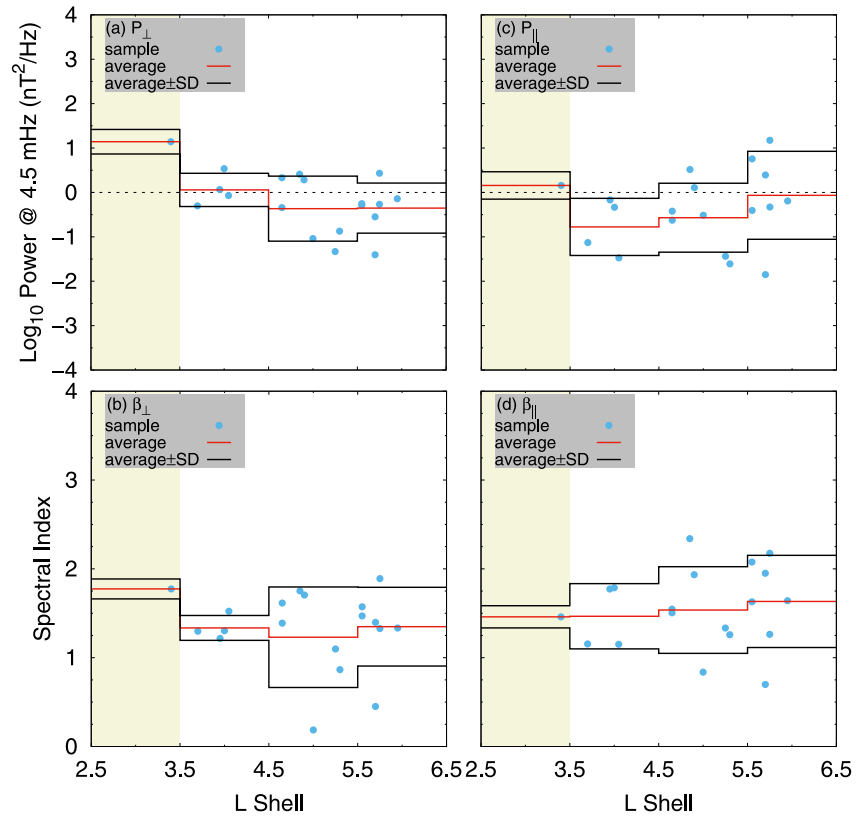
Figure 15. Same as in Figure 7, except during quiet solar wind (QSW). The $2.5 \leq L < 3.5$ bin (it is filled with beige) has one event only, and so the statistics in this bin cannot be considered as reliable. We show this bin only to specify the L shell range in our database of QSW events.

$-20° \leq$ MLAT $< -10°$ bin and $10° \leq$ MLAT $< 20°$ bin, respectively. The MLAT profile of the average transverse power in Figure 16a, on the other hand, is qualitatively dissimilar to the respective power profiles during both CMEs and HSSs. During CMEs and HSSs, the average MLAT profiles of transverse powers are quasi-symmetric with respect to the equator with a minimum in the near equatorial region. The average transverse power during QSW, on the other hand, monotonically decreases with MLAT from an off equatorial maximum in one hemisphere to an off equatorial minimum in the opposite one. The average transverse powers in the reliable bins of Figure 16a are $\langle \log_{10}P_{\perp} \rangle = 0.3$ in the $-20° \leq$ MLAT $< -10°$ bin, $\langle \log_{10}P_{\perp} \rangle = -0.2$ in the $0° \leq$ MLAT $< 10°$ bin, and $\langle \log_{10}P_{\perp} \rangle = -0.5$ in the $10° \leq$ MLAT $< 20°$ bin. A strong north to south asymmetry of an MLAT profile for the average transverse power during QSW may be caused by a combination of the magnetosheath magnetic field pressure dominance over the plasma flow pressure (similar to the situation we discussed in Section 2.8 for CMEs) and the fact that the ULF wave power is low during QSW. Now we can formulate our two conclusions as follows. (a) The average compressional power during QSW has a maximum in the near equatorial MLAT region, similar to that during CMEs and HSSs, and the average power maximum and minima are about 5–10 times and 8–20 times lower during QSW compared to the respective power maxima and minima during CMEs and HSSs. (b) The MLAT profile of the average transverse power during QSW is qualitatively dissimilar to the average transverse power profiles during both CMEs and HSSs. The CME and HSS profiles have near equatorial minima and are quasi-symmetric with respect to the equator, whereas the power during QSW has a strong north to south asymmetry, monotonically decreasing from the off equatorial maximum in one hemisphere to the off equatorial minimum in the opposite one. Quantitatively, the average transverse powers during QSW are about 6–50 times lower compared to the average powers in the respective MLAT bins during CMEs and HSSs.

The average spectral indices in the reliable MLAT bins of Figures 16b and 16d are in the ranges of $\langle \beta_{\perp} \rangle = 1.2$–1.5 and $\langle \beta_{\parallel} \rangle = 1.5$–1.8. Despite the fact that the average indices here are slightly larger than the indices in Sections 3.3–3.7 above, our two conclusions here are still identical to the respective conclusions in Section 3.3.
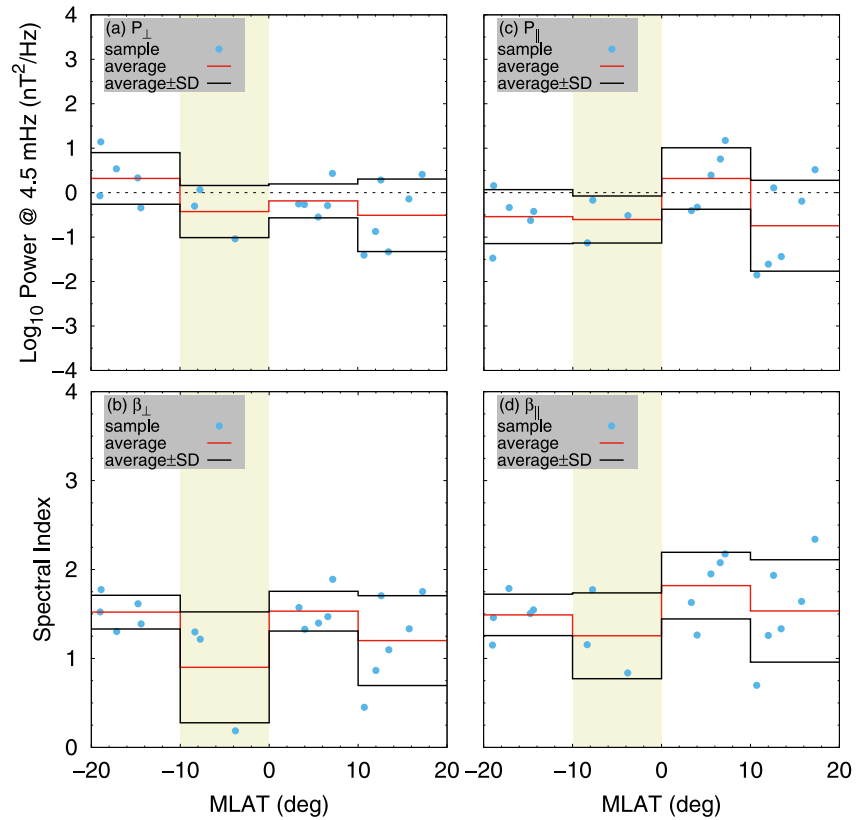
Figure 16. Same as in Figure 8, except during quiet solar wind (QSW). Note that the $-10° \leq$ MLAT $< 0°$ bin (it is filled with beige) has three events only, and so the statistics in this bin are unreliable. We show this bin only to specify the entire MLAT range in our database of QSW events.

3.9. Nonthermal Seed Fluctuations for EMIC Waves

For all the 19 events analyzed during QSW, the ULF wave spectra are well approximated by power laws in the Pc 1–5 frequency range. This indicates that a turbulent energy cascade exists during QSW, similar to that during both the CME and HSS driven events analyzed in Paper 1 and in Section 2, respectively. To estimate the transverse seed power in the Pc 1–2 frequency range during QSW, we use all the QSW events analyzed here. The estimated seed power is in the range of $P_{\perp,seed,QSW} \sim 10^{-4}$–$10^{-1}$ nT^2/Hz. So we conclude that (a) a turbulent energy cascade exists in the Earth's inner magnetosphere during QSW conditions, similar to that during HSSs and CMEs, and (b) the range of the EMIC wave seed power during QSW is similar to that during CMEs, but it is substantially narrower compared to that during the HSSs.

4. Comparison of HSS, CME, and QSW Events

The results of our comparative analyses of the low frequency ULF wave power spectra during HSS, CME, and QSW conditions were presented in Sections 2 and 3 along with the SYM/H index, Kp index, AE index, MLT, L shell, and MLAT statistical analyses there. For convenience, we list our major findings below.

1. The power spectra of the transverse and compressional magnetic field fluctuations during CMEs, HSSs, and QSW are well approximated by power laws $P(f) \sim 1/f^\beta$ in a large frequency range of $f \sim$ mHz - Hz. Because there are no shocks and/or discontinuities in the time series of any of the EMFISIS data analyzed here and in Paper 1, the power law spectra indicate that a turbulent energy cascade exists in the Earth's inner magnetosphere independently of the SW driving conditions. The average spectral indices in the power law fits to the transverse power spectra during HSSs are close to 5/3 of Kolmogorov turbulence if geomagnetic indices are in the ranges of $|$SYM/H$| \lesssim 25$nT, or $Kp \lesssim 5$, or AE $\lesssim 1,000$ nT. The SYM/H index range here is identical to the SYM/H range for Kolmogorov-like turbulence during CMEs, but the above Kp and AE ranges

are substantially wider compared to the respective ranges during CMEs. This shows that Kolmogorov-like turbulence is more common during HSSs compared to that during CMEs and also indicates that the turbulence in the inner magnetosphere is more strongly controlled by the SW conditions than geomagnetic ones.

2. For transverse and compressional powers, the averages of the power law fits at $f_{av} = 4.5$ mHz are in the ranges of $0.1 \leq \langle \log_{10} P_{\perp,HSS}(f_{av}) \rangle \leq 1.6$ and $-0.5 \leq \langle \log_{10} P_{\parallel,HSS}(f_{av}) \rangle \leq 1.5$ during HSSs, and the respective ranges during QSW are $-0.5 \leq \langle \log_{10} P_{\perp,QSW}(f_{av}) \rangle \leq 0.3$ and $-0.8 \leq \langle \log_{10} P_{\parallel,QSW}(f_{av}) \rangle \leq 0.3$, where $P_{\perp}$ and $P_{\parallel}$ are in units of nT²/Hz. So independently of the SW driving conditions (see Paper 1 for CMEs), on average the largest transverse and compressional powers are comparable, and the smallest transverse power dominates the smallest compressional power. The largest average powers during HSSs and CMEs are close, whereas the largest average powers during QSW are about 16–32 times smaller compared to the respective powers during HSSs and CMEs. On average, the spectral indices in power laws are $\langle \beta_{\perp,HSS} \rangle = 1.4$–1.9 and $\langle \beta_{\parallel,HSS} \rangle = 1.5$–2.2 during HSSs, and the ranges during QSW are $\langle \beta_{\perp,QSW} \rangle = 1.2$–1.5 and $\langle \beta_{\parallel,QSW} \rangle = 1.5$–1.8. So the average spectral indices during HSSs and CMEs are close, whereas they are considerably smaller during QSW compared to those during HSSs and CMEs. Independently of the SW driving conditions, the average spectral indices for compressional power are larger than those for transverse power, indicating that the low frequency ULF observations in the inner magnetosphere are dominated by the fluctuations of the fast magnetosonic type.

3. In the -50 nT $\leq$ SYM/H < 0 region, the average ULF wave powers, $\langle \log_{10} P_{\perp,\parallel}(f_{av}) \rangle$, during HSSs and CMEs are close. An external source of ULF waves is clearly seen in the region $0 \leq$ SYM/H < 25 nT during HSSs, where the average compressional power $\left(\langle \log_{10} P_{\parallel,HSS}(f_{av}) \rangle = 1.5 \right)$ dominates the average transverse power $\left(\langle \log_{10} P_{\perp,HSS}(f_{av}) \rangle = 1 \right)$, whereas during CMEs an external source is only seen for SYM/H > 25 nT. The dominance of the average compressional ULF wave power over the average transverse power during the $0 <$ SYM/H $\lesssim 25$ nT geomagnetic conditions may serve as a proxy of HSSs in the upstream SW, whereas the opposite relation between the average powers is an indication of CMEs. In the -25 nT $\leq$ SYM/H < 0 region shared by the QSW, HSS, and CME events, $\langle \log_{10} P_{\perp}(f_{av}) \rangle$ dominates $\langle \log_{10} P_{\parallel}(f_{av}) \rangle$ independently of the SW driving conditions, where both the average transverse and compressional powers during QSW are about an order of magnitude lower compared to the respective powers during CMEs and HSSs.

4. In the $Kp < 5$ region shared by the HSS and CME events, the average ULF wave powers, $\langle \log_{10} P_{\perp,\parallel}(f_{av}) \rangle$, during HSSs and CMEs are close. In the $0 \leq Kp < 3$ region shared by the QSW, HSS, and CME events, $\langle \log_{10} P_{\perp}(f_{av}) \rangle$ dominates $\langle \log_{10} P_{\parallel}(f_{av}) \rangle$ independently of the SW driving conditions, where both the average transverse and compressional powers during QSW are about 3–5 times lower compared to the respective powers during CMEs and HSSs.

5. In the 100 nT $\leq$ AE $< 1,000$ nT region, the average ULF wave powers, $\langle \log_{10} P_{\perp,\parallel}(f_{av}) \rangle$, during HSSs and CMEs are close, whereas the average powers during HSSs are about 3–5 times lower compared to those during CMEs in the region 10 nT $\leq$ AE < 100 nT. In the 10 nT $\leq$ AE < 400 nT region shared by the QSW, HSS, and CME events, the AE profiles of $\langle \log_{10} P_{\perp,\parallel}(f_{av}) \rangle$ during QSW are qualitatively similar to those during HSSs, but not to the profiles during CMEs. Quantitatively, $\langle \log_{10} P_{\perp,\parallel}(f_{av}) \rangle$ during QSW are smaller compared to the respective powers during HSSs by less than a factor of two and about 5–6 times in the 10 nT $\leq$ AE < 100 nT bin and 100 nT $\leq$ AE < 400 nT bin, respectively.

6. The average compressional power during HSSs has a maximum of $\langle \log_{10} P_{\parallel,HSS}(f_{av}) \rangle = 1.3$ in the MLT $= 18$–24 hr bin, whereas the maximum of compressional power during CMEs is located in the MLT $= 12$–18 hr bin. This is because of an additional contribution to the compressional power in the MLT $= 18$–24 hr bin from the external source during HSSs. The average transverse power during HSSs has its maximum of $\langle \log_{10} P_{\perp,HSS}(f_{av}) \rangle = 1.2$ in the MLT $= 12$–18 hr bin, similar to that during CMEs. However, the minimum of transverse power $\left(\langle \log_{10} P_{\perp,HSS}(f_{av}) \rangle = 0.4 \right)$ is observed in the MLT $= 6$–12 hr bin during HSSs, whereas the minimum during CMEs is observed in the MLT $= 0$–6 hr bin. In the MLT $= 6$–12 hr region shared by the QSW, HSS, and CME events, $\langle \log_{10} P_{\perp}(f_{av}) \rangle$ dominates $\langle \log_{10} P_{\parallel}(f_{av}) \rangle$ independently of the SW driving conditions, where the average transverse and compressional powers during QSW are about 4–13 and 6–10 times lower compared to the respective powers during CMEs and HSSs.

7. The average ULF wave powers, $\langle \log_{10} P_{\perp,\parallel}(f_{av}) \rangle$, during HSSs and CMEs are close in the $3.5 \leq L < 5.5$ region, whereas the average powers during HSSs are about 2–2.5 times larger compared to those during CMEs in the highest $5.5 \leq L < 6.5$ bin. In the $3.5 \leq L < 6.5$ region shared by the QSW, HSS, and CME events, the L shell profiles of average compressional power, $\langle \log_{10} P_{\parallel}(f_{av}) \rangle$, during QSW, HSSs, and CMEs are qualitatively similar, where the average compressional power during QSW is about 10–20 times lower compared to the

respective powers during CMEs and HSSs. The L shell profile of average transverse power, $\langle \log_{10} P_\perp (f_{av}) \rangle$, during QSW, however, is qualitatively dissimilar to the respective profiles during both CMEs and HSSs. The CME and HSS transverse power profiles grow with L shell, whereas the QSW profile first decreases and then almost does not depend on L shell. The average transverse powers during QSW are about 2.5–4 and 25–50 times lower compared to the average transverse powers during CMEs and HSSs in the $3.5 \leq L < 4.5$ bin and $5.5 \leq L < 6.5$ bin, respectively.

8. The MLAT profiles of the average ULF wave powers, $\langle \log_{10} P_{\perp,\parallel} (f_{av}) \rangle$, during HSSs and CMEs are qualitatively similar. During QSW, the average compressional power, $\langle \log_{10} P_\parallel (f_{av}) \rangle$, has a maximum in the near equatorial MLAT region, similar to that during CMEs and HSSs, where the power maximum and minima during QSW are about 5–10 and 8–20 times lower compared to the respective power maxima and minima during CMEs and HSSs. The MLAT profile of the average transverse power, $\langle \log_{10} P_\perp (f_{av}) \rangle$, during QSW, however, is qualitatively dissimilar to the respective profiles during CMEs and HSSs. The CME and HSS transverse power profiles have the near equatorial minima and are quasi-symmetric with respect to the equator, whereas the average transverse power during QSW has a strong north to south asymmetry, monotonically decreasing from the off equatorial maximum of $\langle \log_{10} P_{\perp,QSW} (f_{av}) \rangle = 0.3$ in one hemisphere to the off equatorial minimum of $\langle \log_{10} P_{\perp,QSW} (f_{av}) \rangle = -0.5$ in the opposite one. The average transverse powers during QSW are about 6–50 times lower compared to the average transverse powers in the respective MLAT bins during CMEs and HSSs.

9. Independently of the SW driving conditions, a turbulent energy cascade supplies the nonthermal electromagnetic seed fluctuations required for the EMIC wave growth due to relaxation of unstable distributions of the energetic magnetospheric ions. The seed transverse powers of EMIC waves in the Pc 1–2 frequency range are similar during QSW and CMEs, being $P_{\perp,seed,QSW} \sim P_{\perp,seed,CME} \sim 10^{-4}$–$10^{-1}$ nT^2/Hz, whereas the range of seed power during HSSs is substantially wider, being $P_{\perp,seed,HSS} \sim 10^{-5}$–$10^{0}$ nT^2/Hz.

5. Summary

Here, we have extended the scope of the Gamayunov and Engebretson (2021, hereinafter Paper 1) work by analyzing the ULF wave power spectra in the $\sim$ mHz - Hz frequency range in the Earth's inner magnetosphere during HSS and QSW conditions in the upstream SW and comparing our results to the results of Paper 1, where the statistics of ULF wave power spectra during CMEs are presented. This work and Paper 1 are the first attempt to rigorously study the ULF wave power spectra in the inner magnetosphere as a function of different driving conditions in the upstream SW, and the major results of our statistical and comparative analyses can be summarized as follows.

1. During CME, HSS, and QSW conditions in the upstream SW, the magnetic field power spectra of the transverse and compressional fluctuations in the inner magnetosphere are well approximated by power laws in the Pc 1–5 frequency range of $\sim$ mHz - Hz.

2. Independently of the SW driving conditions, on average the largest transverse and compressional powers are comparable, and the smallest transverse power dominates the smallest compressional power. In the spatial and geomagnetic index regions shared by the HSS and CME events, the largest average powers and the average spectral indices during HSSs and CMEs are close. On the other hand in the spatial and geomagnetic index regions shared by the QSW, HSS, and CME events, the largest average powers and the average spectral indices during QSW are $\sim$20–30 times and up to $\sim$1.6 times smaller compared to the respective average powers and indices during HSSs and CMEs.

3. Independently of the SW driving conditions, the average spectral indices for compressional power are larger than those for transverse power, indicating that the low frequency ULF fluctuations in the inner magnetosphere are dominated by the fluctuations of the fast magnetosonic type.

4. The dominance of the average compressional power over the average transverse power for the low frequency ULF waves during the $0 < $ SYM/H $\lesssim 25$ nT geomagnetic conditions may serve as a proxy of HSSs in the upstream SW, whereas the opposite relation between the average powers is an indication of CMEs.

5. Independently of the SW driving conditions, a turbulent energy cascade from low frequencies in the ULF wave frequency range into the higher frequency range exists in the Earth's inner magnetosphere, supplying the nonthermal electromagnetic seed fluctuations required for the growth of EMIC waves due to instabilities of the energetic RC ion distributions.

Data Availability Statement

CDF files of Van Allen Probes EMFISIS data are available at http://emfisis.physics.uiowa.edu. The SYM/H index and AE index data are available at https://omniweb.gsfc.nasa.gov/form/omni_min.html, and the *Kp* index data are available at https://omniweb.gsfc.nasa.gov/form/dx1.html. The events during HSS and QSW conditions analyzed here are available in the Gamayunov and Engebretson (2022) data set.

References

Anderson, B. J., & Fuselier, S. A. (1994). Response of thermal ions to electromagnetic ion cyclotron waves. *Journal of Geophysical Research*, *99*, 19413. https://doi.org/10.1029/94ja01235

Borovsky, J. E., & Denton, M. H. (2006). Differences between CME-driven storms and CIR-driven storms. *Journal of Geophysical Research*, *111*(A07S08). https://doi.org/10.1029/2005JA011447

Borovsky, J. E., Elphic, R. C., Funsten, H. O., & Thomsen, M. F. (1997). The Earth's plasma sheet as a laboratory for flow turbulence in high-β MHD. *Journal of Plasma Physics*, *57*(1), 1–34. https://doi.org/10.1017/S0022377896005259

Cornwall, J. M., Coroniti, F. V., & Thorne, R. M. (1971). Unified theory of SAR arc formation at the plasmapause. *Journal of Geophysical Research*, *76*, 4428–4445. https://doi.org/10.1029/ja076i019p04428

El-Alaoui, M., Richard, R. L., Ashour-Abdalla, M., Goldstein, M. L., & Walker, R. J. (2013). Dipolarization and turbulence in the plasma sheet during a substorm: THEMIS observations and global MHD simulations. *Journal of Geophysical Research: Space Physics*, *118*(12), 7752–7761. https://doi.org/10.1002/2013JA019322

Gamayunov, K. V., Elkington, S., & Engebretson, M. (2020). Strongest electromagnetic ion cyclotron waves observed by the NASA RBSP Mission, 1 October 2012 to 7 June 2014 [Dataset]. RBSP. https://doi.org/10.25810/fze6-7391

Gamayunov, K. V., & Engebretson, M. J. (2021). Low frequency ULF waves in the Earth's inner magnetosphere: Statistics during coronal mass ejections and seeding of EMIC waves. *Journal of Geophysical Research: Space Physics*, *126*(8), e2021JA029247. https://doi.org/10.1029/2021JA029247

Gamayunov, K. V., & Engebretson, M. J. (2022). ULF wave events during HSSs and quiet solar wind conditions in the upstream SW observed by the two Van Allen Probes from 1 October 2012 through 7 June 2014 [Dataset]. Harvard Dataverse. https://doi.org/10.7910/DVN/VO4VVH

Gamayunov, K. V., Engebretson, M. J., & Elkington, S. R. (2020). EMIC waves in the Earth's inner magnetosphere as a function of solar wind structures during solar maximum. *Journal of Geophysical Research: Space Physics*, *125*, e2020JA027990. https://doi.org/10.1029/2020ja027990

Gamayunov, K. V., Engebretson, M. J., Zhang, M., & Rassoul, H. K. (2014). Model of electromagnetic ion cyclotron waves in the inner magnetosphere. *Journal of Geophysical Research: Space Physics*, *119*(9), 7541–7565. https://doi.org/10.1002/2014JA020032

Gamayunov, K. V., Engebretson, M. J., Zhang, M., & Rassoul, H. K. (2015). Source of seed fluctuations for electromagnetic ion cyclotron waves in Earth's magnetosphere. *Advances in Space Research*, *55*(11), 2573–2583. https://doi.org/10.1016/j.asr.2015.02.024

Gamayunov, K. V., & Khazanov, G. V. (2007). Effect of oblique electromagnetic ion cyclotron waves on relativistic electron scattering: Combined Release and Radiation Effects Satellite (CRRES)-based calculation. *Journal of Geophysical Research*, *112*(A07220). https://doi.org/10.1029/2007JA012300

Gonzalez, W. D., Tsurutani, B. T., Gonzalez, A. L. C., Smith, E. J., Tang, F., & Akasofu, S.-I. (1989). Solar wind-magnetosphere coupling during intense magnetic storms (1978–1979). *Journal of Geophysical Research*, *94*, 8835. https://doi.org/10.1029/ja094ia07p08835

Hudson, M. K., Denton, R. E., Lessard, M. R., Miftakhova, E. G., & Anderson, R. R. (2004). A study of Pc-5 ULF oscillations. *Annales Geophysicae*, *22*(1), 289–302. https://doi.org/10.5194/angeo-22-289-2004

Kletzing, C. A., Kurth, W. S., Acuna, M., MacDowall, R. J., Torbert, R. B., Averkamp, T., et al. (2013). The Electric and Magnetic Field Instrument Suite and Integrated Science (EMFISIS) on RBSP. *Space Science Reviews*, *179*, 127–181. https://doi.org/10.1007/S11214-013-9993-6

Lorentzen, K. R., McCarthy, M. P., Parks, G. K., Foat, J. E., Millan, R. M., Smith, D. M., et al. (2000). Precipitation of relativistic electrons by interaction with electromagnetic ion cyclotron waves. *Journal of Geophysical Research*, *105*, 5381–5389. https://doi.org/10.1029/1999ja000283

Murphy, K. R., Inglis, A. R., Sibeck, D. G., Rae, I. J., Watt, C. E. J., Silveira, M., et al. (2018). Determining the mode, frequency, and azimuthal wave number of ULF waves during an HSS and moderate geomagnetic storm. *Journal of Geophysical Research: Space Physics*, *123*(8), 6457–6477. https://doi.org/10.1029/2017JA024877

Murphy, K. R., Inglis, A. R., Sibeck, D. G., Watt, C. E. J., & Rae, I. J. (2020). Inner magnetospheric ULF waves: The occurrence and distribution of broadband and discrete wave activity. *Journal of Geophysical Research: Space Physics*, *125*(9), e2020ja027887. https://doi.org/10.1029/2020ja027887

Mursula, K., Bräysy, T., Niskala, K., & Russell, C. T. (2001). Pc1 pearls revisited: Structured electromagnetic ion cyclotron waves on polar satellite and on ground. *Journal of Geophysical Research: Space Physics*, *106*(A12), 29543–29553. https://doi.org/10.1029/2000JA003044

Sandanger, M., Soraas, F., Aarsnes, K., Oksavik, K., & Evans, D. S. (2007). Loss of relativistic electrons: Evidence for pitch angle scattering by electromagnetic ion cyclotron waves excited by unstable ring current protons. *Journal of Geophysical Research*, *112*(A12213). https://doi.org/10.1029/2006JA012138

Takahashi, K., & Anderson, B. J. (1992). Distribution of ULF energy ($f < 80$ mHz) in the inner magnetosphere: A statistical analysis of AMPTE CCE magnetic field data. *Journal of Geophysical Research: Space Physics*, *97*(A7), 10751–10773. https://doi.org/10.1029/92JA00328

Takahashi, K., Yumoto, K., Claudepierre, S. G., Sanchez, E. R., Troshichev, O. A., & Janzhura, A. S. (2012). Dependence of the amplitude of Pc5-band magnetic field variations on the solar wind and solar activity. *Journal of Geophysical Research: Space Physics*, *117*(A4). https://doi.org/10.1029/2011JA017120

Thorne, R., & Horne, R. (1994). Energy transfer between energetic ring current H^+ and O^+ by electromagnetic ion cyclotron waves. *Journal of Geophysical Research*, *99*, 17275. https://doi.org/10.1029/94ja01007

Weygand, J., Kivelson, M. G., Khurana, K., Leinweber, H., Thompson, S., McPherron, R., et al. (2005). Plasma sheet turbulence observed by Cluster II. *Journal of Geophysical Research*, *110*. https://doi.org/10.1029/2004JA010581